Applications of High-resolution High-precision Spectral Observations in Solar Physics

Hao Ran

August 21, 2024

Contents

1 Introduction

With but few exceptions, quantitatively researches of the Sun are based on the interpretation of spectroscopic observations. Whether such data are collected at radio, visual, or X-ray wavelengths, their interpretation rest upon our ability. First, to identify the process by which the radiation is produced, second, to interpret the radiation in terms of local plasma conditions at the place of origin, and third, to organize the different plasma regimes observed at different wavelengths in proper relationship (*Zirin 1988* [62]). With the development of observational technology, solar spectral observations are gradually moving towards higher resolution and precision, providing increasingly better data for solar physics research.

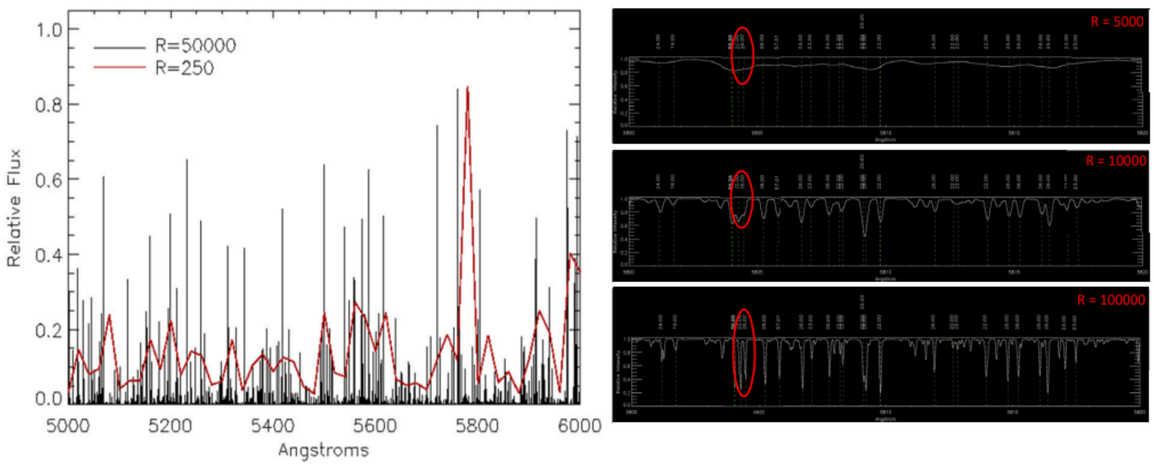

Figure 1: Left: A small portion of the spectrum from a ThAr hallow cathode lamp as recorded at high ($R = 50000$, black) and low ($R = 250$, red) resolution. Right: Synthetic solar spectra computed in the same wavelength range with different resolution as indicated on each one. Figure directly adopted from *Giarrusso et al. (2018)* [20].

The advantages in using high-resolution spectroscopy to analyze light from stars are numerous (*Giarrusso et al. 2018* [20]). Here we only present a brief introduction, details will be discussed in the following sections. First, for spectral line identification, as shown in the left panel of Figure 1 which records a small portion of the spectrum from a ThAr hallow cathode lamp at high ($R = 50000$, black) and low ($R = 250$, red) resolution. It is clear that most of the lines are wasted at low resolution because of blending, and so can not be detected. The right panel shows a further example of synthetic solar spectra computed in the same wavelength with different resolution. Only in high resolution can we distinguish between near lines of different elements, and then correctly determine stellar metallicity.

High resolution spectroscopy also enables the detection of isotopes in stellar atmospheres by measuring the isotopic shifts in spectral lines (*Catanzaro et al. 2006* [12]). These shifts are generally less than 0.01 nm, necessitating a spectral resolution greater than 50000 at a wavelength of 500 nm.

The measurement of velocity fields, which can only be accurately estimated using high-resolution spectroscopy via the Doppler effect, is crucial for probing stellar plasmas. When a star moves away from or towards the observer, its spectrum is redshifted or blueshifted by $\Delta\lambda_D = \lambda v/c$ relative to a synthetic spectrum. Analyzing the spectral line profile allows us to distinguish the various chaotic or ordered mass flows, such as microturbulence, oscillations, or winds within cosmic objects (*Gary 2021* [22]). For example, a star's rotational velocity can only be measured if the corresponding line profile exceeds the instrumental profile $\Delta\lambda = \lambda/R$. Consequently, the minimum measurable velocity field is approximately $v = c\lambda/\Delta\lambda = c/R$, which equates to 1200 km/s at $R = 250$ and 3 km/s at $R = 100000$. Similarly, spectral resolution plays a vital role in determining a star's gravity through collisional line broadening, which results from the interaction between emitters and surrounding electrons, ions, or neutral particles that modify atomic energy levels.

When a star has a magnetic field, the atomic level split into sublevels, causing spectral lines to split into a series of Zeeman components. These components are classified as π if $\delta m = 0$, σ_b (blu eshifted) if $\Delta m = +1$, and σ_r (red shifted) if $\Delta m = -1$, where m is the magnetic quantum number.

The average wavelength separation between the σ_b and σ_r components, $\Delta\lambda_\sigma$, is proportional to the strength of the magnetic field $|B|$, and is given by:

$$\Delta\lambda_\sigma = 2 \times 4.67 \times 10^{-13} \lambda^2 g_{eff} |B|,$$

where λ in Å, g_{eff} is the effective Landé factor, and B is in Gauss. To measure the intensity of the stellar magnetic field accurately, the spectral resolution must be high enough to satisfy $\Delta\lambda \leq \Delta\lambda_\sigma$. For example, at $\lambda = 500nm$ and $g_{eff} = 1$, the minimum field strength than can be detected is 85 T with a resolution of $R = 250$ and 0.21 T with $R = 100000$.

This review is organized as follows. In section 2, we introduce how the Zeeman effects and Doppler velocity measurements are applied in high-resolution spectral observations of the Sun. The methods of profile analysis are also discussed. In section 3, we present the typical wavebands and their research significance in solar physics. The wavebands are catogorized by their formation region, from the photosphere to the corona. We finally introduce some existing solar observatories and their high-resolution spectral observations in section 4.

2 High-resolution Spectral Observations of the Sun

2.1 Methods

2.1.1 Application of the Zeeman Effects

The Zeeman effect refers to the splitting of spectral lines due to the presence of an external magnetic field. Figure 2 shows a typical example of a spectral line observed in a sunspot, which is split into three components under the influence of the photosphere magnetic field. This observation clearly shows the Zeeman effect. In the absence of an external magnetic field, emission is observed as a single spectral line and is dependent only on the *principle quantum number* of the initial and final states. With the existence of a magnetic field, the principle number of each state is split into several substates, resulting in permitted transitions that have frequencies above the below the original frequency. The number of split levels is given by $(2 \times L + 1)$, where L is the *orbital angular momentum quantum number*. The degree of the splitting is proportional to the strength of the magnetic field. Note that not all transitions are allowed. The selection rule for the Zeeman effect is $\Delta m_l = 0, \pm1$, where m_l is the *magnetic quantum number* (See Figure 3).

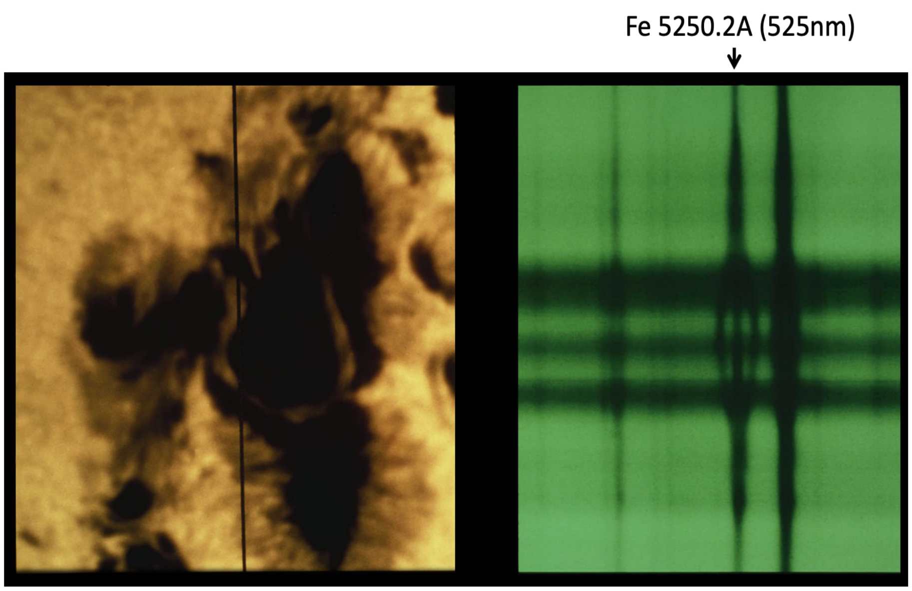

Figure 2: Observation of the Zeeman effect. The black vertical line on the white light image (left) shows the location of the slit for the spectrum which took the spectrum (right). The spectral line is split into three components, which clearly shows the Zeeman effect.

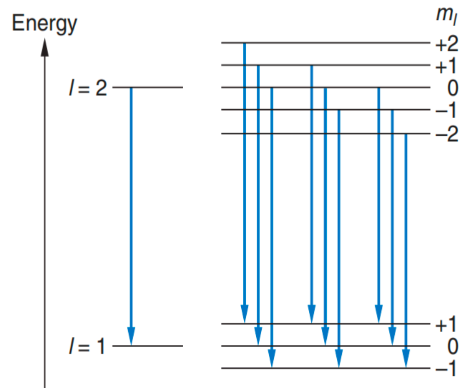

Figure 3: Energy-level splitting for singlet levels $l = 2$ and $l = 1$. Each level is split into $2l + 1$ terms. The rule $\Delta m_l = 0, \pm 1$ restricts the number of possible transitions to the nine shown.

The Zeeman effect that occurs for spectral lines resulting from a transition between singlet states is called the *normal Zeeman effect*, while that which occurs when the total spin of either the initial or final states, or both, is nonzero is called the *anomalous Zeeman effect*. There is no fundamental difference between the two types. In the anomalous Zeeman effect, each energy is split into $2j + 1$ levels. The energy shift relative to the position of the non-splitting line is:

$$\Delta E = g m_j \frac{e\hbar B}{2m_e} = g m_j \mu_B B,$$

here, g is the *Landé g-factor*, m_j is the *magnetic quantum number*, e is the *elementary charge*, $\hbar$ is the *reduced Planck constant*, B is the *magnetic field strength*, m_e is the *electron mass*, and μ_B is the *Bohr magneton*. The Landé g-factor is given by:

$$g = 1 + \frac{j(j+1) + s(s+1) - l(l+1)}{2j(j+1)},$$

where j is the *total angular momentum quantum number*, s is the *spin quantum number*, and l is the *orbital angular momentum quantum number*. Note that for $s = 0$, $j = 1$, and $g = 1$, the above equation gives the splitting in the normal Zeeman effect.

Since that we have roughly understood the principle, we can now give an example of using the Zeeman effect to calculate the magnetic field of the Sun. Suppose that the sodium D_1 line (589.8 nm) emitted in a particular region of the solar disk is observed to split into a four-component Zeeman effect. The wavelength difference $\Delta\lambda$ measured between the two outer components is 0.022 nm. What is the strength of the magnetic field in this region of the Sun?

The Sodium D_1 line is emitted by a transition from the $3^2P_{1/2}$ to $3^2S_{1/2}$. We can compute the ΔE values of each level as follows:

For the $3^2P_{1/2}$ level:

$$g = 1 + \frac{1/2(1/2+1) + 1/2(1/2+1) - 1(1+1)}{(2)(1/2)(1/2+1)} = 2/3,$$

the energy shift is:

$$\Delta E = (2/3)(\pm 1/2)(5.79 \times 10^{-9} \text{ eV/G})B.$$

For the $3^2S_{1/2}$ level:

$$g = 1 + \frac{1/2(1/2+1) + 1/2(1/2+1) - 1(1+1)}{(2)(1/2)(1/2+1)} = 2,$$

the energy shift is:

$$\Delta E = (2)(\pm 1/2)(5.79 \times 10^{-9} \text{ eV/G})B.$$

The longest-wavelength line ($m_j = -1/2 \rightarrow +1/2$) undergoes a net energy shift of:

$$-1.93 \times 10^{-9}\ B - 5.79 \times\ 10^{-9}\ B = -7.72 \times 10^{-9}\ B \text{ eV}.$$

The shortest-wavelength line ($m_j = +1/2 \to -1/2$) undergoes a net energy shift of:

$$1.93 \times 10^{-9}\ B + 5.79 \times 10^{-9}\ B = 7.72 \times 10^{-9}\ B \text{ eV}.$$

The total energy difference between the two photons is:

$$\Delta E = -1.54 \times 10^{-8}\ B \text{ eV}.$$

Since $\lambda = c/f = hc/E$, we have $\Delta\lambda = -(hc/E^2)\Delta E = 0.022$ nm, where $E = hc/\lambda$. Then, we can derive that $B = 0.51$ T $= 5100$G, which is a typical value for photosphere magnetic field strength.

2.1.2 Doppler Velocity Measurements

Doppler velocity measurement of the solar atmosphere refers to investigating the motion of solar material by analyzing the shifts in the wavelength of spectrum emitted or absorbed by that material. These measurements are crucial for understanding various dynamic processes in the solar atmosphere, including solar winds, flares, and oscillations. Doppler velocity measurement method is a powerful tool for studying the 3-D velocity field of the solar atmosphere. For example, *Taro Morimoto & Hiroki Kurokawa (2003)* [37] developed a method to measure the 3-D velocity field of disappearing filaments. Their method consists of two steps: (1) the line-of-sight is obtained by calculating the H-α line profile of the filament and by measuring the Doppler shifts. The tangential velocity is obtained by tracing the motions of the structures.

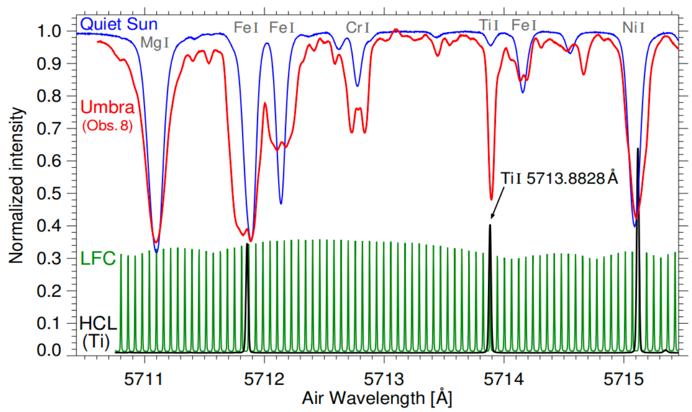

Figure 4: Spectra observed with LARS at around 5713 Å. The spectra were observed in the quiet Sun at disk center (blue), and in the sunspot umbra (red). The ions of the spectra lines are stated in gray color. The emission spectra of the laser frequency comb (LFC, green) and the titanium hollow cathode lamp (HCL, black) are also plotted for showing the calibration of absolute wavelengths and Doppler shifts. Figure directly adopted from *Löhner-Böttcher et al. (2018)* [35]

.

To illustrate how Doppler velocity measurement is used in solar physics, we take the work of *Löhner-Böttcher et al. (2018)* [35] as an example. The authors directly measured the Doppler velocities of the darkest part of sunspot umbrae with an unprecedented accuracy and precision using the Laser Absolute Reference Spectrograph (LARS) at the German Vacuum Tower Telescope. The spectral Ti I line at 5173.9 Å is selected since it becomes stronger in cooler atmosphere and returns no Zeeman effect due to the Landé g-factor of zero.

Figure 4 shows an overview of the spectra observation. To obtain a very good spectral precision, high resolution was essential. At a wavelength of $\lambda = 5714$ Å and a full width at half maximum ($\Delta\lambda \approx 8$ mÅ) of the instrumental profile, the authors obtain a resolution of $\lambda/\Delta\lambda > 700000$. A laser frequency comb served for the calibration of the spectrograph and the determination of the absolute wavelength scale of the solar spectrum. The solar spectrum and the frequency comb spectrum were recorded in an alternating order, enabling a quasi-simultaneous wavelength calibration.

A detailed view of the Ti I 5713.9 Å line is shown in Figure 5. To obtain a high precision of the measurement of the laboratory wavelength of the Ti I 5713.9 Å line, the authors used the hollow

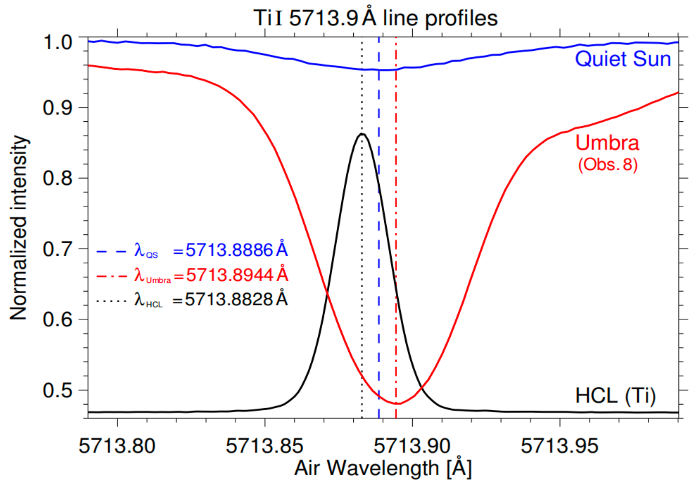

Figure 5: High-resolution observations of the Ti I 5713.9 Å line. The quiet Sun spectrum (blue) and umbral spectrum (red) are compared with the emission spectrum from the hollow cathode lamp (HCL, black). The center positions of fits to the line core are marked as blue dashed (quiet Sun), red dashed-dotted (umbra), and black dotted (HCL) lines. The corresponding wavelengths of the center positions are also marked on the left side of the plot. Figure directly adopted from *Löhner-Böttcher et al. (2018)* [35].

cathode lamp (HCL) as a reference. The good agreement between the line profile and a Voigt function yielded a central wavelength of $\lambda_0 = 5713.8828$ Å with an error of around 0.05 mÅ, which could be translated into an uncertainty of $\sigma_{\lambda_0} = 2.6$ m/s. With the laboratory wavelength λ_0 (or λ_{HCL}), it was possible to calculate the Doppler shift of the observed wavelength position λ of the solar spectral line. The line-of-sight Doppler velocity v_{los} was calculated by:

$$v_{los} = c \cdot (\lambda - \lambda_0)/\lambda_0 - v_{grs},$$

where c is the speed of light, $v_{grs} = +633$ km/s is the gravitational redshift (12.1 mÅ at $\lambda = 5713.9$ Å).

2.1.3 Profile Analysis

We expand the content of this section to the spectrum profile analysis of stellar atmospheres, not just the solar atmosphere. A group of key parameters (temperature, surface gravity, global metallicity, individual element abundances) can be obtained from a stellar spectrum.

Effective surface temperature of a star In the early 1890s, Wilhelm Wien investigated thermodynamics and coined the term 'black body' for an ideal radiator. He discovered that the wavelength of maximum radiation is inversely proportional to the temperature of the black body. This relation is named Wien's law:

$$\lambda_{max} = \frac{W}{T},$$

where λ_{max} is the peak wavelength, T is the effective temperature of the star, and W is the Wien constant (2.898×10^3 for λ_{max} in meters and T in Kelvins).

Figure 6 shows an example of how to calculate the effective temperature of a star using Wien's law. This is an actual stellar spectrum, so it approximates a black body and has absorption lines in it rather than being a perfect continuum Planck curve. Each small portion of the spectrum contains a large quantity of information. The peak wavelength of the star is 458.0 nm, corresponding to a temperature of around 6300 K.

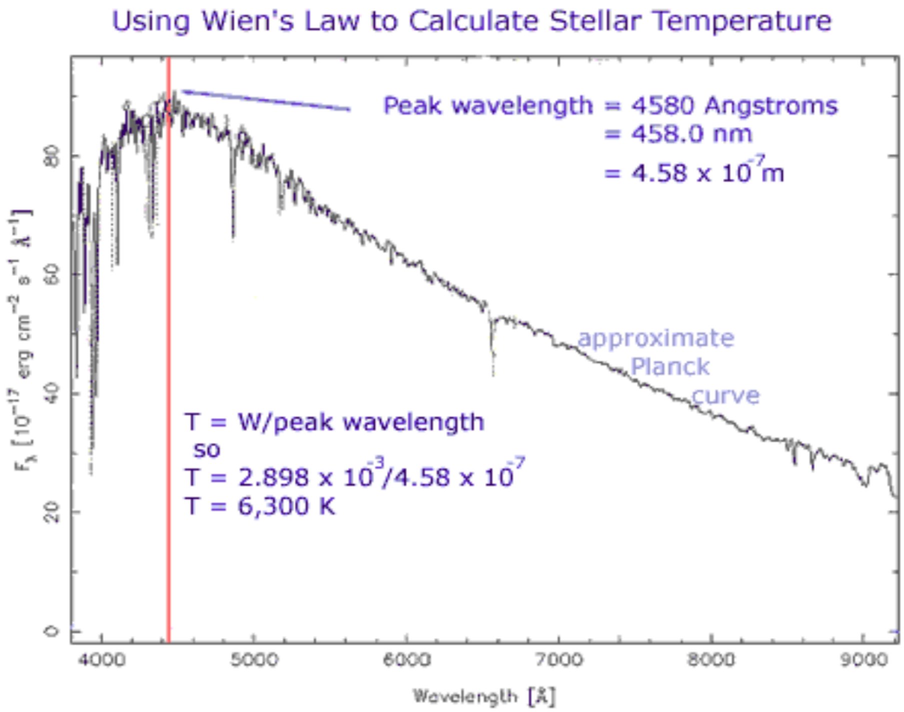

Figure 6: An example showing how to calculate the effective temperature of a star using Wien's law.

Line Equivalent Width The equivalent width W_λ is defined as the width, in wavelength units, of a rectangular strip of spectrum having the same area as the absorption line:

$$W_\lambda = \int_0^{\text{inf}} \frac{I_{\lambda,0} - I_\lambda}{I_{\lambda,0}} d\lambda = \int_0^{\text{inf}} (1 - e^{-\tau\lambda}) d\lambda,$$

where τ_λ is the optical depth. The optical depth can be defined with opacity and the distance travelled:

$$\tau_\lambda = \int_0^s \kappa_\lambda \rho ds = \int_0^s n\sigma_\lambda ds,$$

where n is the volume density of particles (atoms and ions) and σ_λ is the cross-section for the interaction which, in the case of discrete absorption lines, corresponds to bound-bound transitions, that is electronic trasition between different energy levels. The line equivalent width represents the width of a rectangular region, centered on the spectral line, that would absorb the same total amount of light (or emit the same total amount of light in the case of an emission line) as the actual spectral line does.

Figure 7 shows four absorption lines with the same equivalent widths but different shapes. If two absorption lines have the same equivalent width but different shapes, this implies that the total amount of absorption (or the area under the curve) is the same, but the distribution of that absorption across wavelengths is different. This might be caused by different broadening mechanisms or different optical depths. The equivalent width is a convenient measure of the strength of an absorption line. What all instrument record is the convolution of the intrinsic line shape with the instrumental broadening function; if the latter is broader than the intrinsic width of the absorption line recorded, much of the information encoded in the line profile itself is lost. However, the equivalent width is invariant to the convolution, and is thus a conserved quantity. Some stellar parameters of interest can be deduced from measurements of the line equivalent widths, particularly the relative fractions of atoms and ions in different excitation and ionisation stages and the relative abundances of different elements.

Line Broadening Process In stellar atmospheres, there are a number of physical processes that broaden the absorption lines. The two main processes are: 1. Natural broadening, due to the uncertainty ΔE in the energy of the upper atomic level k. 2. Doppler broadening, due to the motions of the absorbers.

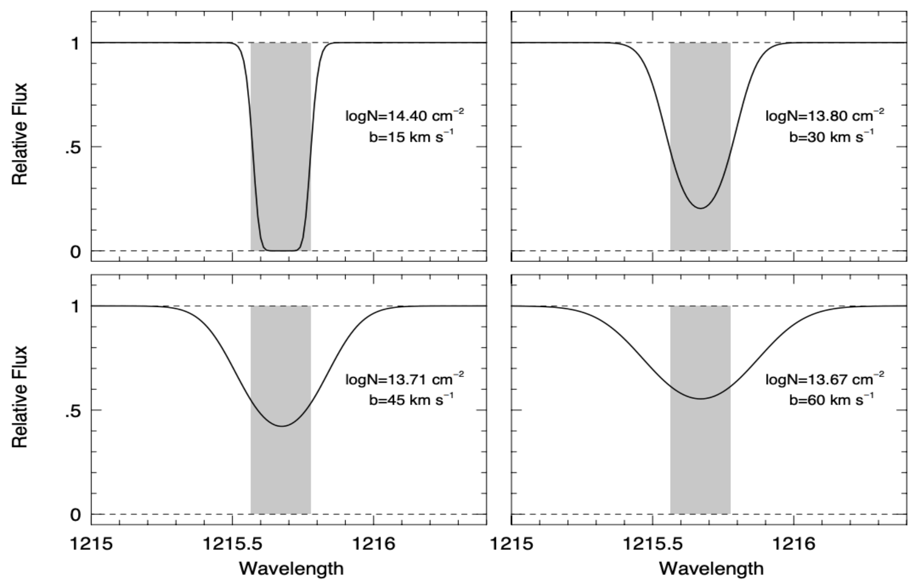

Figure 7: Four absorption lines with the same equivalent width (shaded in gray) but different widths, as measured by the value of Doppler broadening parameter b. N (cm^{-2}) is column density, defined as the number of absorbers in a column of unit corss-section area.

Natural broadening arises from the inherent uncertainty in the energy levels of atoms or molecules, which is a consequent of the Heisenberg unvertainty principle. This principle states that the uncertainty in energy (ΔE) is inversely related to the uncertainty in time (Δt), i.e., $\Delta E \cdot \Delta t \geqslant \hbar/2$. When an atom or molecule emits or absorbs a photon, the excited state has a finite lifetime. The shorter this lifetime, the greater the uncertainty in the energy of the photon, leading to a broadening of the spectral line. This effect is also known as lifetime broadening. The line shape due to natural broadening is described by a Lorentzian profile, characterized by a central peak with long, slowly decaying tails. Natural broadening is typically quite small and is more significant in very precise measurements, such as in atomic clocks or high-resolution spectroscopy.

Doppler broadening occurs due to the relative motion between the source of the spectral line (such as atoms or molecules) and the observer. This motion causes a shift in the frequency of the emitted or absorbed radiation, resulting in a spread of the observed frequencies. Doppler broadening produces a Gaussian profile, characterized by a symmetric bell-shaped curve. The width of the line is related to the temperature of the gas and the mass of the particles, with higher temperatures and lighter particles leading to broader lines. Doppler broadening is typically larger than natural broadening in many astrophysical environments, especially in cases involving high temperatures or light atoms, such as hydrogen.

The Curve of Growth We define the column density N as the number of absorbers in a column of unit cross-section area:

$$N = \int_0^s n ds.$$

The curve of growth (COG) describes the relationship between the equivalent width W_λ of an absorption line and the column density N of absorbing atoms.

Figure 8 shows an example of COG. As shown in the figure, a COG typically has three distinct phases;

- **Linear (Optically thin) regime**: In the initial phase where the column density is low, the line is optically thin. This means that the strength of the absorption line (equivalent width) increases linearly with the column density. Each additional absorber contributes directly to the line strength because photons can easily travel through without being absorbed by another atom first. In this regime, the COG is a straight line, indicating a proportional relationship. The absorption line profile in this regime is linear.

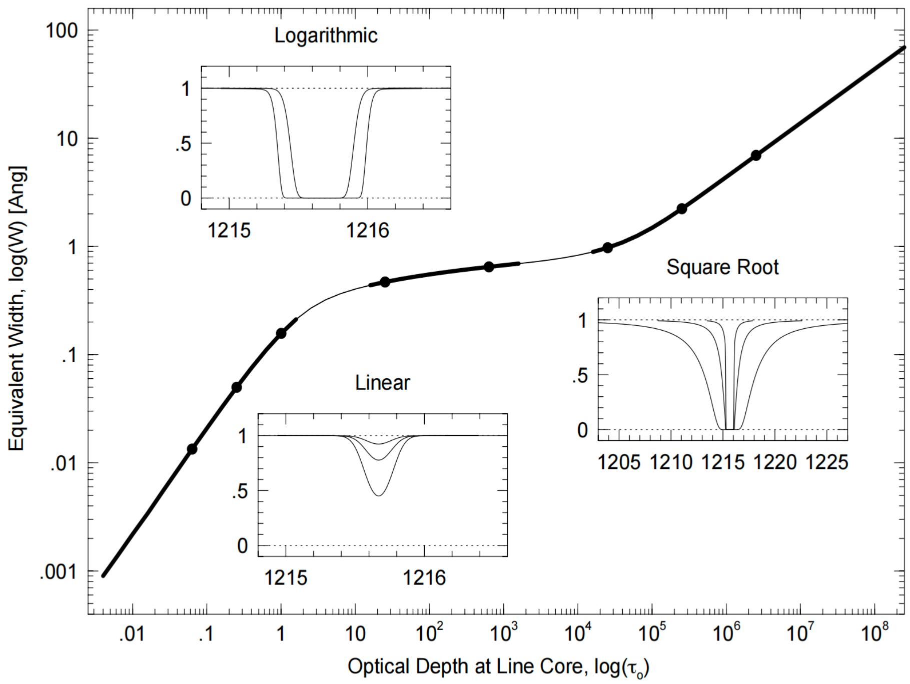

Figure 8: Example of a curve of growth. The three regimes discussed, the linear, flat, and damping part of the COG are shown by thicker curves. Corresponding line absorption profiles are shown for each regime and their locations on the COG are marked with filled dots.

- **Flat (Saturated) regime**: As the column density increases further, the absorption line becomes saturated. In this phase, the central part of the line absorbs most of the light, and additional absorbers contribute less effectively because the core of the line is already absorbed. The equivalent width increases more slowly with increasing column density, showing a flat curve. The absorption line profile in this regime is logarithmic.
- **Damping wing (Optically thick) regime**: At very high column densities, the absorption line is not only saturated at the core but also begins to extend into the damping wings. These wings are caused by natural broadening and contribute to the line's equivalent width. In this regime, the equivalent width again increases more rapidly with column density, but the COG is in the form of a broader, more gradual rise. The wings of the line, which were negligible at lower column densities, now dominate the absorption process. The absorption line profile in this regime is square root.

The COG is crucial for interpreting the results of spectroscopic observations, particularly in astrophysics and atmosphereic studies. By comparing observed equivalent widths with the COG, observers can determine the column density of different elements or ions in stars, interstellat clouds, or other astronomical objects.

Measurements of Stellar Parameters from Spectral Lines Nowadays, the analysis of stellar spectra is generally conducted by comparing the observed spectrum with a suite of theoretical ones computed from a stellar model atmosphere. In such models, each atmospheric layer is involved in the formation of the line profiles and contributes to the final spectrum. Here we give several examples.

(1). **Spectral lines as pressure indicators.**

Stars above the main sequence of the HR diagram have higher luminosity and lower photospheric pressure than stars on the main sequence due to their expansion. Indeed, pressure effects are often referred to as luminosity effects. As is explained previously, pressure adds to the natural broadening constant to give characteristic broad wings to the absorption lines. From the measurement of these wings, astronomers can obtain the value of *surface gravity*, or *log g*, where g is the gravitational acceleration (cms^{-2}). For example, $log\ g = 3$ at the surface of the Earth, $log\ g \simeq 4.5$ for main sequence stars. In supergiants, $log\ g$ varies by three orders of magnitude, from $log\ g \simeq 3.5$ in O5 I stars to $log\ g \simeq 0$ in M2 I red supergiants.

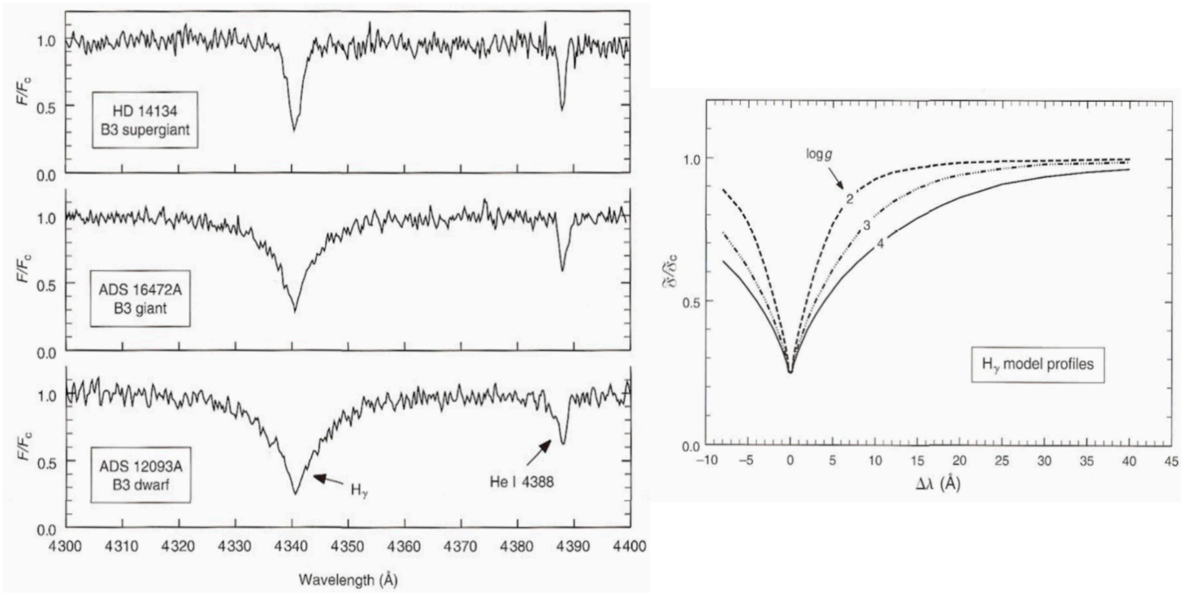

Figure 9: Left: Pressure variations in the profile on the Hγ line in B3 stars of different luminosity classes. The effect arises from the pressure dependence of the linear Stark effect (electric field equivalent of the Zeeman effect), the broadening of the $n = 2$ and $n = 5$ energy levels of neutral hydrogen due to presence of an external electric field provided by nearby ions. Right: Model profiles of the Hγ line of the Balmer series for different values of surface gravity.

Figure 9 shows that the pressure sensitivity in the hydrogen lines of the Balmer series is one of the classical luminosity indicators in early-type stars. The difference of the line profile in the Hγ line between different stars is shown in the left panel. The model profiles are shown in the right panel. Note that the gravity dependence rapidly diminishes with temperature below $T_{eff} \simeq 10000K$.

Some other strong metal lines also show pressure-broadening wings in the spectra of cooler stars. We present an example in the left panel of Figure 10. Since pressure diagnostics are always temperature sensitive, it is often useful to make a simultaneous solution for T_{eff} and $log\ g$. This can be achieved if we have two lines that have different responses to the two variables, as in the case shown in the right panel of Figure 10. Each curve in this gravity-temperature diagram is computed for a fixed Fe abundance, while varying $log\ g$ at a given T_{eff} (or vice versa) to recover the obseerved equivalent width. The crossing point is then the solution, which includes the correct effective temperature and surface gravity.

(2). **Abundance determinations from metal absorption lines**

Another important free parameter that we can determine from the rigorous analysis of absorption lines is: the abundance of element under consideration. By comparing the observed spectrum with model spectra computed for a range of values of, for example, Fe / H, the abundance of iron in the stellar photosphere can be deduced (See Figure 11). Higher-resolution observations are required for more accurate abundance determinations.

2.2 Typical Wavebands and Their Research Significance

Figure 12 is probably the best-known figure in solar physics, showing the average quiet Sun temperature distribution and the regions where various spectral features are formed. The spectra indicated are due to H, H^-, C, Si, Fe, $CaII$, and $MgII$. We have listed in Figure 13 the most common elements found in the Sun and the point of spectrum where the absorption/emission line is found, its width, features to be observed, and its height above the photosphere. In this section, we will introduce some typical wavebands that are often used to observe different layers of the solar atmosphere.

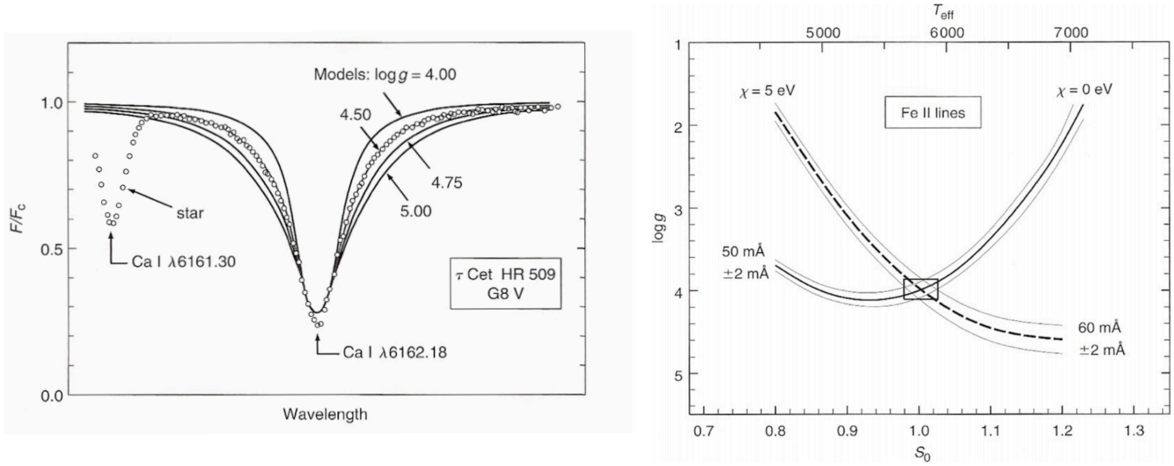

Figure 10: Left: Fitting theoretical line profiles to the Ca I $\lambda 6162$ observed line, which gives a measure of the surface gravity: $log\ g = 4.50$. Right: Gravity-Temperature diagram for the equivalent widths of two Fe II absorption lines of different excitation potential as indicated.

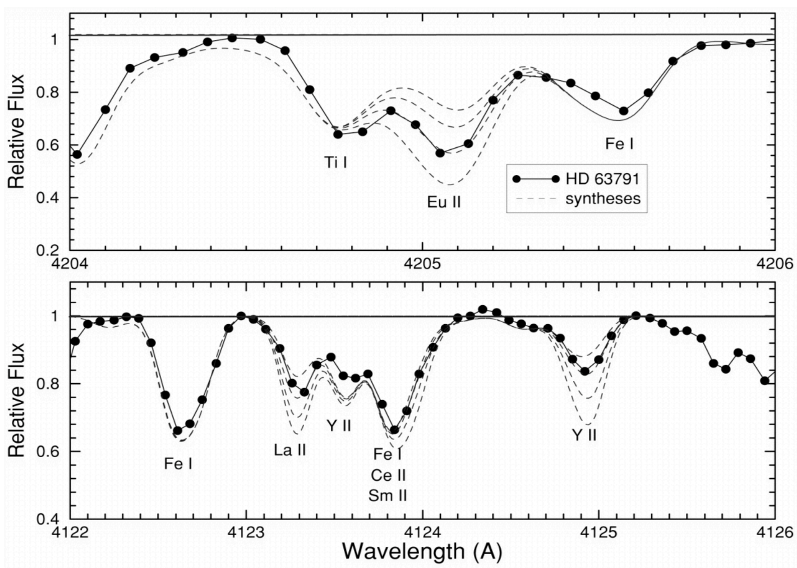

Figure 11: Example of spectral synthesis from which element abundances are deduced. Filled circles represent the observed spectrum, while the lines show the the model spectra. All the model spectra share a same effective temperature $T_{eff} = 4725K$, a same surface gravity $log\ g = 1.70$, and a same value of microturbulence $\xi 1.60 kms^{-1}$, but differ in the values of abundances of the elements of interest. The solid line is deemed to fit best. The spectrum used for this abundance analysis has resolving power of $R = \lambda/\Delta\lambda \simeq 20000$ and signal-to-noise raio of around 100. Figure reproduced from *Burris et al. (2000)* [10].

2.2.1 Photosphere

The Sun's *photosphere* is the out shell of the Sun from which light is radiated, appearing as a light, glowing surface. This layer is about 500 km thick and has a temperature ranging from 4500 to 6000 K. The photosphere is composed of convection cells called granules, which are about 1000 km in diameter and have a lifespan of about 8 to 20 minutes. The photosphere also exhibits sunspots, which are cooler and darker regions caused by intense magnetic activity. A continuous spectrum, punctuated by absorption lines from a variety of elements, can be observed from the photosphere. The spectrum reveals details of the Sun's composition and physical conditions. In this section, we will go

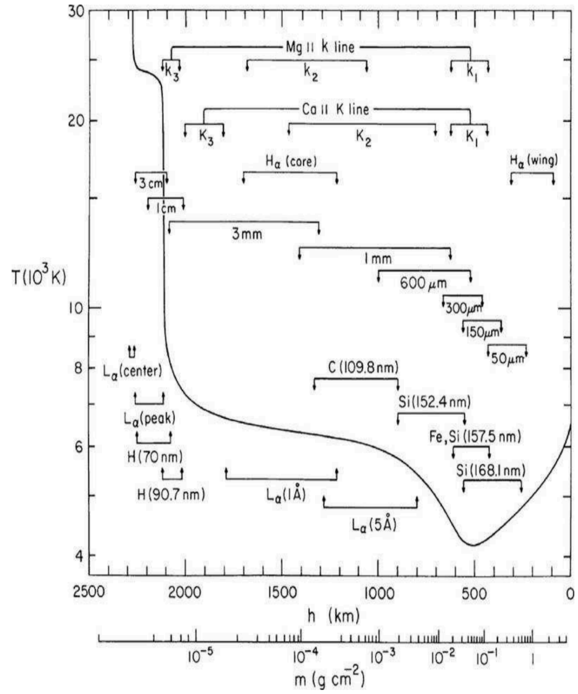

Figure 12: The average quiet-Sun temperature distribution derived from EUV continuum, and observations of different spectral lines. The approximate depths where the various continua and lines originate are indicated. Figure directly adopted from *Vernazza et al. (1981)* [56].

through some typical wavelengths that are often used to observe the photosphere and their research significance.

Ion I (Fe I) Lines Iron lines crowd the solar spectrum from ultraviolet (UV) to infrared (IR) wavelengths. Lines of neutral ions are among the most popular diagnostic lines for the solar photosphere in particular for the photospheric magnetism (e.g., *Rutten et al. 1982* [47]). The Fe I 6173 Å line, for example, is one of the most important lines for photospheric magnetism. It is used by many instruments including the Helioseismic and Magnetic Imager (HMI; *Scherrer et al. 2012* [50]) onboard the Solar Dynamics Observatory (SDO) and the the Polarimetric and Helioseismic Imager (PHI; *Solanki et al. 2020* [52]) on board the Solar Orbiter (SO). Figure 14 shows an HMI observation of the latest photospheric magnetism based on the Fe I 6173 Å line.

There are multiple advantages of using the Fe I 6173 Å line for photosphere observations. First, the line is very sensitive to the Zeeman effect, which allows for accurate measurements of the magnetic field strength and direction in the photosphere (*Auer et al. 1977* [5]). Second, the profile of the Fe I 6173 Å line is relatively clean. It only has one blend 0.6 Å away from its line center identified as La II, the influence brought by this blend is acceptable. Third, this line has relatively strong absorption features, which makes it easier to detect and analyze than other weaker lines(*Norton et al. 2006* [39]). *Norton et al. (2006)* [39] compared the performance of Fe I 6173 Å line with Ni I 6768 Åline in observing the photospheric magnetic field. They claimed that the Fe I 6173 Å line is overall better than the Ni I 6768 Åline in terms of field strength determination, flux direction determination, and inclination angle determination.

Besides the Fe I 6173 line, there are many other Fe I lines that are used to observe the photosphere. For example, the Fe I 6302 Å line is a promising candidate for observing the photospheric magnetic field (*Norton et al. 2006* [39]). According to *Socass-Navarro et al. (2008)*, the combined analysis of the Fe I 6302 Å line and 5250 Å line also yields a significant determination of the quiet-Sun magnetic properties.

Wavelength (nm)	Name	Species	Equivalent width (nm) Disk Centre	Region	Height above Photosphere (Km)	Temp (K)
Soft X-rays				Corona	>5000	2,000,000
121.57	Lyman a	H		Upper chromosphere	2200	20,000
155		C IV		Transition region	2500	100,000
279.54	k	Mg II	2.2	UV emission, high chromosphere	500-1600	
280.23	h	Mg II	2.2			
388.36	(CN band head)	CN	0.03 (index)	Photosphere, magnetic field tracer		
393.36	K	Ca II	2	Chromosphere, flares, prominences	600-1500	
396.85	H	Ca II	1.5	Chromosphere, flares, prominences	1000-2000	
430.79	G band	CH (Fe I, Ti II)	0.72	Photosphere, flares, magnetic field tracer		
517.27	b2	Mg I	0.075	Low chromosphere		
518.36	b1	Mg I	0.025			
525.02		Fe I	0.007	Photosphere, magnetic fields (g=3)		
537.96		Fe I	0.0079	Medium photosphere		
538.03		C I	0.0025	Low photosphere		
557.61		Fe I		Photosphere, velocity fields (g=0)		
587.56	D3	He I		Chromosphere, flares, prominences		
589	D2	Na I	0.075	Upper photosphere, low chromosphere, prominences		
589.59	D1	Na I	0.056	Upper photosphere, low chromosphere, prominences		
612.22		Ca I		Photosphere, magnetic fields (g 1.5)		
630.25		Fe I	0.0083	Photosphere, magnetic fields (g=2.5)		
656.28	C (Ha)	H I	0.41	Chromosphere, prominences, flares	1250-1700	
676.78		Ni I		Photosphere, oscillations		
769.89		K I		Photosphere, oscillations		
777.42		O I	0.0066	High photosphere		
849.8	Calcium 'infrared triplet'	Ca 1	0.13	Low chromosphere, prominences		
854.21	Calcium 'infrared triplet'	Ca I	0.37	Low chromosphere, prominences		
866.2	Calcium 'infrared triplet'	Ca I	0.27	Low chromosphere, prominences		
868.86		Fe I	0.014	Photosphere, magnetic fields (g=1.7)		
1006.37		FeH		Umbral (only) magnetic fields (g=1.22)		
1083.03		He I	0.003	High chromosphere		
1281.81	H Paschb	H I	0.19	Chromosphere		
1564.85		Fe I	0.0035	Photosphere, magnetic fields (g=3)		
1565.29		Fe I	0.003	Photosphere, magnetic fields (g=1.8)		
2231.06		Ti I		Umbral (only) magnetic fields (g=2.5)		
4652.55	H Pfundb	H I		Chromosphere, electric fields		
4666.24		CO		High photosphere, thermal structure		
12318.3		Mg I		High photosphere, magnetic fileds (g=1)		

Figure 13: The most common elements in the Sun and the wavelength (nm) where the absorption line is found within the spectrum, and the features to be observed.

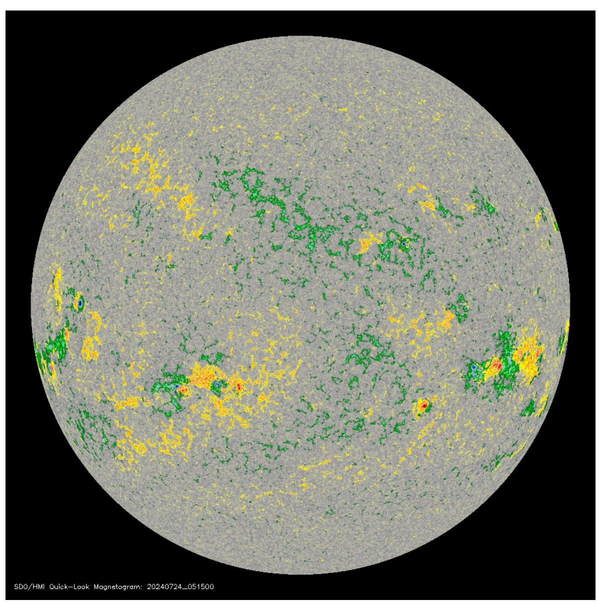

Figure 14: HMI observation of the photospheric magnetic field at 2024.07.24T05:15:00. Positive field values are green and blue, negative field values are yellow and red.

Sodium (Na) I D1 5896 Å Line The Na I D1 5896 Å line, though with great potential in solar physics research, has long been a difficult line to observe and model. Doppler wavelength shifts, *p*-mode oscillations, and other small-scale dynamical processes can bring strong profile line fluctuations

(*Edmonds et al. 1983* [16]). Other affects, such as temperature and magnetic field strength, can also influence the associated Na I D1 line depths (*Athay et al. 1969* [4]). The formation height of the Na I D1 5896 line core has also long been in debate. *Aimanova & Gulyaev (1976)*[1] estimated the core formation height of the Na I D1 5896 line to be between 1300 and 1700 km with slitless spectrograms. This is above the formation height of Ca II K core line ($\approx$ 1200 km) and overlaps with that of the Hα line ($\approx$ 1500 km). However, observations indicate that the Na I D1 line has little in common with their Ca II K or Hα counterparts. *Eibe et al. (2001)* [17] suggested that the formation height varies depending on the local temperature and/or velocity. They estimate a formation height of less than 900 km, suggesting that the Na I D1 emission is formed in the upper photosphere.

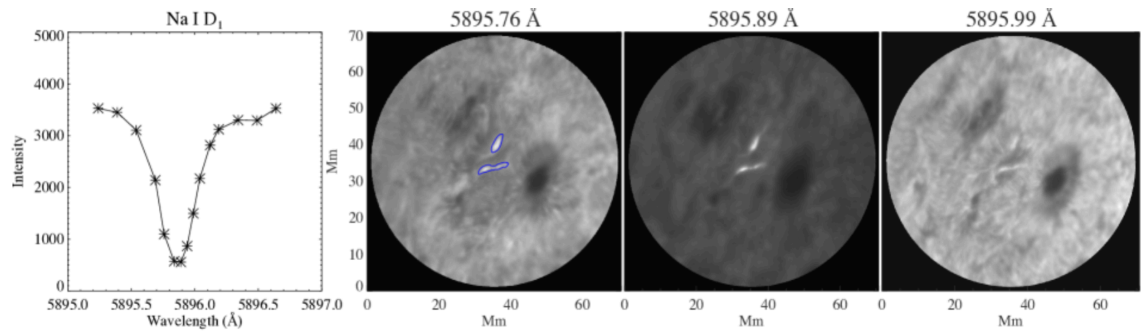

Figure 15: Left: The Na I D1 line profile of a quiet solar region. Right: Na I D1 wing and core images at selected wavelength ranges. The blue contours indicate the upper and lower flare ribbons of a flare. The figure is directly adopted from *Kuridze et al. (2016)* [27].

Na I D1 line can be used to study flares, which is a sudden and intense burst of radiation and energy emanating from the Sun's surface. *Kuridze et al. (2016)*, for example, have presented spectroscopic observations of the Na I D1 line in an M3.9 flare (See Figure 15) and compared their findings with radiative hydrodynamic simulations. They found that during the flare the Na I D1 line goes into emission and a central reversal is formed. On the other hand, Na I D1 line observations yield marked asymmetry between the blue and red line wings: sampling the Sun in the blue wing shows normal granulation, where hot, bright granules are surrounded by cooler, darker intergranular lanes; whereas sampling the Sun in the red wing displays reversed granulation, which appears as dark granules surrounded by bright intergranular lanes at higher altitudes (*Rutten et al. (2011)* [48]). Furthermore, due to the sensitivity to Zeeman effect, the Na I D1 line can also be used to map the magnetic field in the solar atmosphere (*Edmonds et al. 1983* [16]). In quiet Sun regions, the Na I D1 line can help identify subtle oscillations and wave phenomena, contributing to the understanding of the solar atmosphere's underlying physics and the energy transfer from the photosphere to the chromosphere (*Rutten et al. (2011)* [48]). The Na I D2 line, with a wavelength of around 5889 Å , is the other line of the sodium D-line doublet. In conjunction with the Na I D1 line, the Na I D2 line provides comprehensive diagnostic capabilities for studying the Sun's atmospheric structures and dynamics (*Alsina et al. 2021* [2]).

2.2.2 Chromosphere and Transition Region

The Sun's *chromosphere* is a distinct layer above the photosphere and below the corona, extending about 2000 to 3000 kilometers. It is characterized by a reddish flow, best seen during solar eclipses, due to the emission of H-α light. Temperatures on the chromosphere increases with altitude, ranging from around 6000 K at the base to about 20,000 K at the top. This layer is also the site of spicules, which are dynamic and narrow jets of gas, and prominences, which are large, bright loops of plasma.

Above the chromosphere lies the *transition region*, which is a thin layer of the Sun's atmosphere that separates the cooler chromosphere from the hotter corona. The temperature in the transition region rises rapidly from around 20,000 K to about 1 million K over a distance of a few hundred kilometers. Physical processes in the transition region are not well understood, but is believed to play a crucial role in the heating of the corona and the acceleration of the solar wind. The transition region emits strong ultraviolet radiation, showing rapid changes in temperature and density. In this section, we will introduce some typical wavelengths that are often used to observe the chromosphere and transition region. Their research significance will also be discussed.

Helium I D_3 The He I D_3 line (5876 Å) is generally formed in the upper chromosphere, and is sensitive to the local magnetic field. The He I D3 line is also indirectly affected by the heating of the transition region and corona, since it is resulting from a transition that occurs between levels in the triplet system of neutral helium. These levels are generally populated via an ionization-recombination mechanism under the influence of EUV radiation originating in the transition region and corona (*Libbrecht 2019* [32]). In Figure 16 we show raster scan of He I D_3 line in a flux emergence region. Since the He I D_3 line is usually weak on the solar disk, a continuum correction is necessary. This line also suffers from multiple telluric blends and some solar blends (see the right panel of Figure 16). *Libbrecht et al. (2017)* introduced a method to remove the telluric blends and presented their observations of Ellerman bombs with He I D_3 and He I 10830 Ålines.

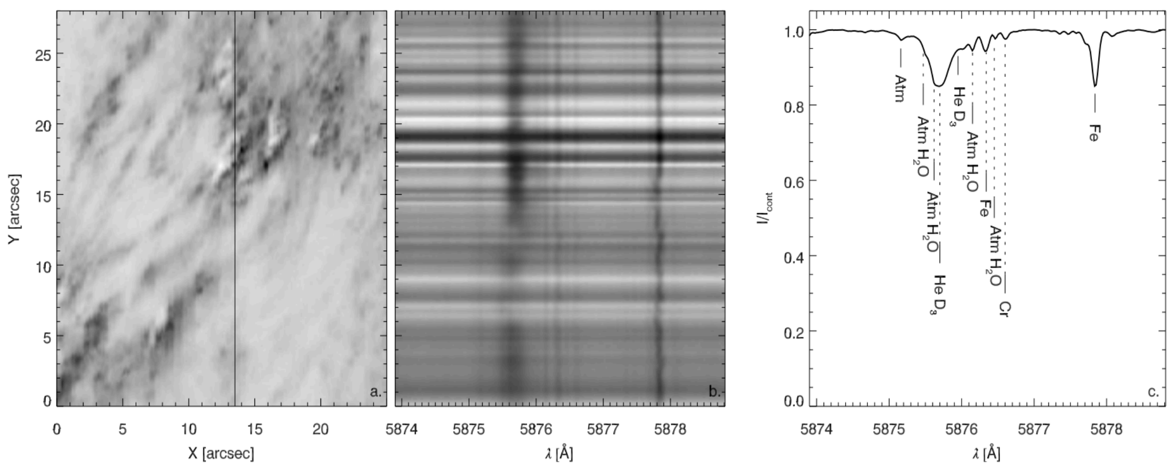

Figure 16: The He I D_3 line in a flux emergence region. The left panel shows the continuum-corrected line core raster scan at this wavelength, the middle panel shows the spectrum of He I D_3 corresponding to the vertical line on the left panel, the right panel presents the average spectrum as shown in the middle panel. Telluric lines are marked with 'Atm'. Figure directly adopted from *Libbrecht (2019)* [32].

The He I D_3 line can be used to observe prominences and filaments. Prominences are large arcade-like structures which appear above the solar limb, while filaments are the on-disk features of prominences which appear dark against the continuum backgroud. The prominence observation in He I D_3 is very weak (compared with Hα observations), thus a proper scaling is needed if one wants to distinguish prominences from this line. Panels (a - c) of Figure 17 show an example of a prominence as observed in the Hα and He I D_3 wavebands. Spicules are thin tube-like chromospheric plasma structures which occur nearly everywhere on the Sun. They are capable of transporting mass and energy between photosphere and corona, and are believed to play an important role in coronal mass supply and heating (e.g., *De Pontieu et al. 2011*). An example of spicule observations in He I D_3 is given in panels (d - f) of Figure 17.

Many telescopes and instruments provide high-resolution observations of He I D_3. The Richad B. Dunn Solar Telescope (DST) is a 76 cm telescope located at Sacramento Peak in New Mexico. It is equipped with an He I D_3 prefilter, which allows it to take He I D_3 images with spectral tuning. The Swedish 1m Solar Telescope (SST, *Scharmer et al. 2003* [49]) is located on the island of La Palma, Spain. It operates TRIPPEL, which is capable of observing three spectral regions simultaneously, meaning that He I 10830 Åand He I D_3 can be observed co-temperarily (e.g., *Libbrecht et al. 2017* [33]). The spectral resolution of TRIPPEL is 200000, which promises the high-quality observations of He I D_3.

Calcium II H & K The Ca II H (3968.469 Å) and K (3933.663 Å) resonance lines was first employed to study fine structures in the solar chromosphere in the early work of *Jensen & Orrall (1963)* [25],

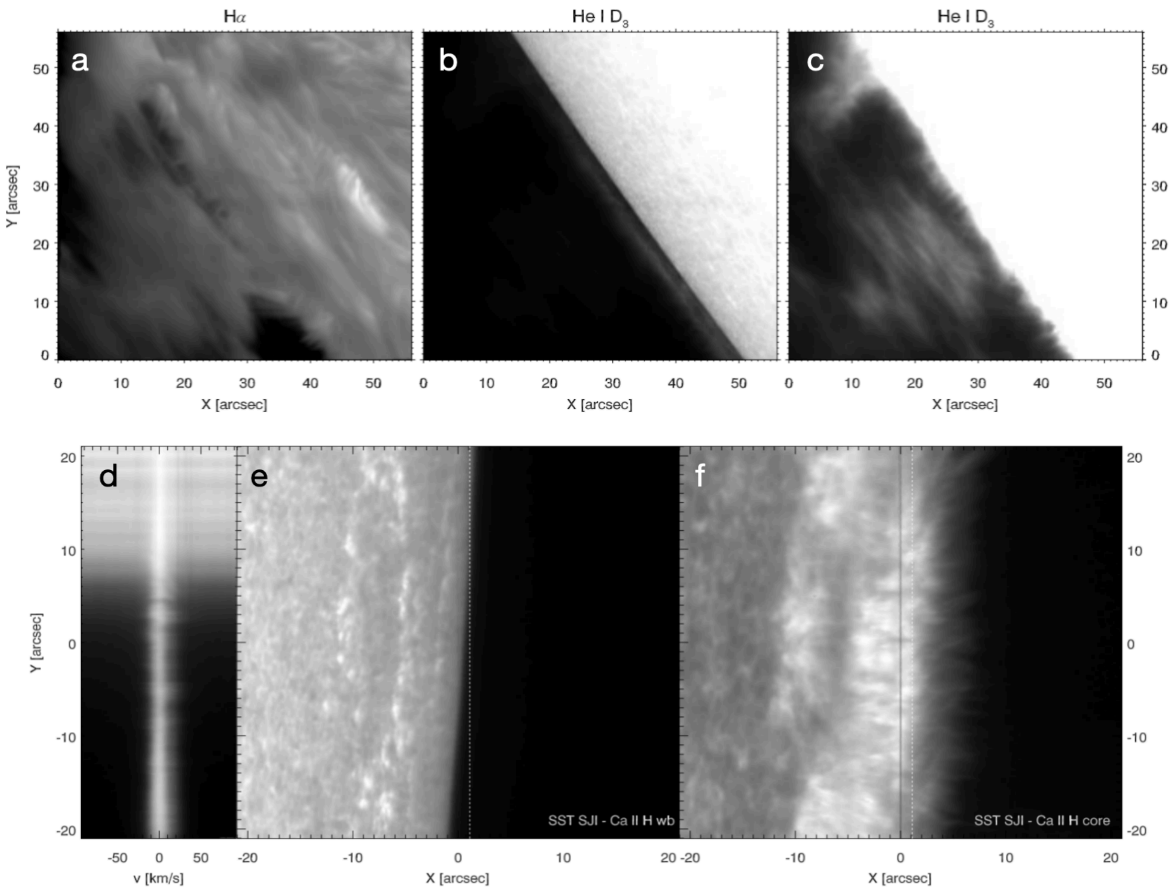

Figure 17: Prominence and Spicules observed in He I D_3 line. The first row shows prominence observed in Hα (a), in He I D_3 (b), and in He I D_3 with proper scaling (c). The second row shows spicules observed in He I D_3 (left spectrum), slit-jaw images in Ca II H continuum (middle) and core (c).

who elucidated aspects of the relationships between chromospheric K line structure and photospheric fine structure, and identified the oscillation nature of the K line variability. Figure 18 presents the absorption lines in the spectrum of Calcium II K and H showing the different regions where we should be observing the emission to see maximum line height details. As is seen, the central region of the K line is called K3 and the two smaller absorption regions are called K1. Each region shows a specific height of the chromosphere (see Figure 12). This is exactly mirrored in the H line. The two Calcium lines should be thought of as a doublet like the sodium doublet, with the only difference being how the transitions are made with the two outer shell electrons. Unlike other diagnostically important chromospheric lines such as Mg II h and k lines that reside in the ultraviolet part of the spectrum, the Ca II H and K lines are formed in the violet part of the visible spectrum and are thus more accessible to ground-based observations. Figure 19 shows the features that can be observed at the Ca II K line, including umbra and penumbra, bright ring, plages, and supergranulations. Umbra refers to the central dark region of sunspots, and penumbra refers to the lighter region surrounding the umbra. Within a developing active region (sunspot group) tiny spots form initially without a developed penumbra and are called pores. Active regions can contain either a single spot or a great number and can last from only a day up to 60 days. The bright ring is an area of brightening around penumbra. The discovery of the bright ring explains the missing energy due to suppression of convective energy transport by underlying magnetic fields. Chromospheric faculae can be observed anywhere on the solar disc and they are an extension of the photospheric faculae into the chromosphere. The supergranulation cells are large scale convective horizontal flow, where material flows outwards from the centre and downward flow has been observed at the boundaries. The flow carries both polarities to the boundaries (*Zirin 1988* [62]). K grains refer to the 'intranetwork bright points' found in the quiet sun. They originate from exclusively within cell interiors in quiet areas of the solar surface. Other phenomenon, such as

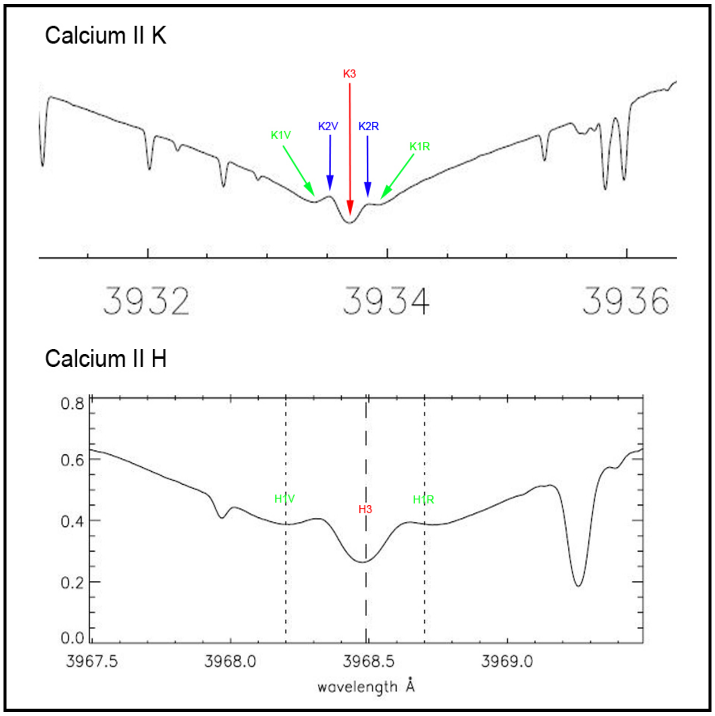

Figure 18: The regions of Ca II K and H line where different heights above the photosphere can be observed.

Ellerman bombs and filaments, can also be observed at the Ca II K line, but appear more faint and less defined than in the Hα window.

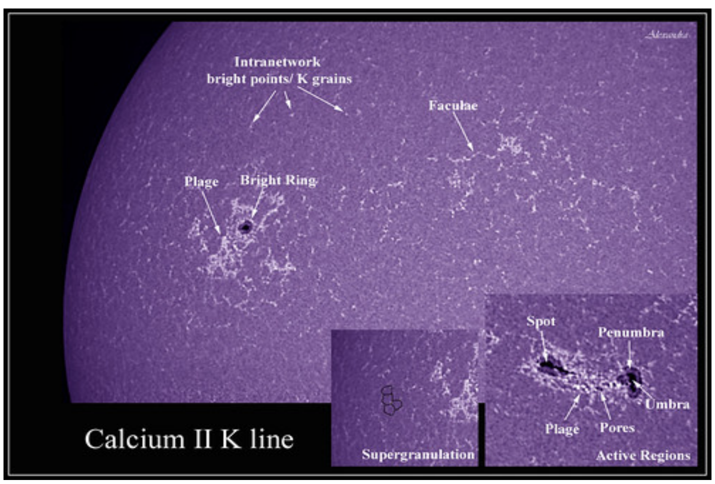

Figure 19: Features that can be observed at Ca II K line. The photograph is taken using a Coronado CaK PST telescope (40mm) and an Imaging Source DMK41 monochrome camera with false colour added.

The H and K line wings are formed in the photosphere with their opacity following local thermal equilibrium (LTE) conditions (*Rutten et al. 2004* [46]). They were used to obtain the temperature stratification of the upper photosphere (*Rouppe van der Voort 2002* [55]), and to investigate the granulation actions in both observation and simulation (*Leenaarts & Wedemeyer-Böhm 2005* [28]). The H and K line cores are formed in the chromosphere and cover a narrow spectral range of ~ 0.4 Å. Note that observations of H and K cores suffer from a strong contamination of the photospheric signal coming from the wings. The K line is also very sensitive to the magnetic field. If magnetic fields are present, absorption is less (more light is transmitted) with weaker magnetic fields showing as darker areas. Therefore, moderately strong magnetic field shows up as bright regions in our images but with the exception of very strong magnetic field, such as in a sunspot where they appear very dark.

Hydrogen alpha Hydrogen alpha (hereafter referred to as Hα) is a specific wavelength at 656.281 nm in the red part of the visible spectrum. A hydrogen atom emits or absorbs a photon at this wavelength when an electron transitions between the second energy level (n=2) and the third energy level (n=3). The Hα line is one of the most popular lines for studying the chromosphere and its energetic events, such as filaments, Ellerman bombs, flares, and spicules (*Carlsson et al. 2019* [11]). Figure 20 (a) shows the differences of the Sun in Hα and white light. Hα observations present more details of the chromosphere. Filaments appear as elongated dark structures against the solar disk (see Figure 20 (b)) in Hα window. When viewed from the edge of the Sun against the dark background of space, filaments appear bright and glowing and are called prominences (see Figure 20 (c)). The brightness is a result of the emission of light by the cooler and denser plasma. Plages are bright and patchy regions in the chromosphere, which mark the sites of active regions and sunspot groups (see Figure 20 (d)). Weak flares, also known as Ellerman bombs or tiny micro-flares, also appear bright, making them easily be confused with plages. However, flares (see Figure 20 (e)) are unmistakable and involves a sudden brightening within a sunspot group often as multiple ribbons that resemble flows of white-hot lava. They can last from a few minutes to hours and change in both intensity and area. Figure 20 (f) shows spicules, which are jets of hot gas between 3,000 to 10,000 km high, seen in profile. They rim the solar circumference like "orange fur". These events leave spectral signatures in the H α intensity profiles, which can be used to investigate the fine-scale structure and temporal evolution of the chromosphere. For example, *Vissers et al. (2019)* [57] combined the observations from the Swedish 1-m Solar Telescope (SST) and the Atmospheric Imaging Assembly (AIA) on board the Solar Dynamics Observatory (SDO) at Hα for developing a detection algorithm for Ellerman bombs.

Due to the complexity of the chromosphere, it is difficult to fully interpret the formation of the Hα line in the chromosphere. On the one hand, the assumption of local thermodynamic equilibrium (LTE) is not always valid in the chromosphere. Non-LTE conditions mean that the population of energy levels in hydrogen atoms is influenced by the radiation field over a larger region, complicating the modeling of the H-alpha line formation. On the other hand, radiative transfer through the chromosphere and the corona is extremely complex due to the non-LTE conditions and the 3D structures of the chromosphere. *Leenaarts et al. (2012)* [29] used advanced radiation-MHD simulations and 3D radiative transfer calculations to investigate the Hα line formation in the chromosphere. They found that the Hα line opacity is more sensitive to mass density than to temperature. This sensitivity implies that the Hα line core intensity correlates with the average formation height: the higher the formation height, the lower the intensity. From the formation perspective, the reasons that make the Hα line is such a good window to observe the Sun are: (1) it has so much opacity in its line core so that it always forms in the low plasma-beta region where the magnetic field dominates; (2) the low mass of the Hydrogen atom makes the line wide, so that the velocity field only has little influence on the fixed-wavelength line core intensity. Instead, it is the variation of the mass density caused by the magnetic field, waves, and shocks that gives rise to the structures of the Hα line. *Tarr et al. (2019)* [54] compared the Atacama Large Millimeter Array (ALMA) 3 mm emissions and Hα solar observations, and confirmed that a strong correlation exists between the Hα line width and the 3 mm brightness temperature. They also found a bimodal relation between the two diagnostics, with shallower slope in cooler regions and steeper slope in hotter regions. The origin of the bimodal distribution remains unknown, but does hold for the observations.

To observe the Hα line with high spatial and spectral resolution, many efforts have been made by the solar physics community. High-resolution imaging spectroscopy in solar physics has relied on Fabry-Pérot interferometers (FPI) in recent years. For example, *Hu et al. (2022)* [24] introduced a tunable narrow-band imager with high spectral resolution based on a FPI they designed to observe the Sun at Hα wavelength, and have shown the first results they obtained from the instrument plus a 65 cm solar telescope. The FPI has a bandpass (FWHM) of 0.09 Åand a free spectral range of 3.85 Å. However, FPI systems get technically challenging and expensive for telescopes larger than 1-m class. To overcome this, *Beck et al. (2018)* [7] introduced the design and utilization of the Interferometric BIdimensional Spectrometer (IBIS) for high-resolution solar observations. They use a subtractive double pass (SDP) technique, which enhances spectral and spatial resolution by passing

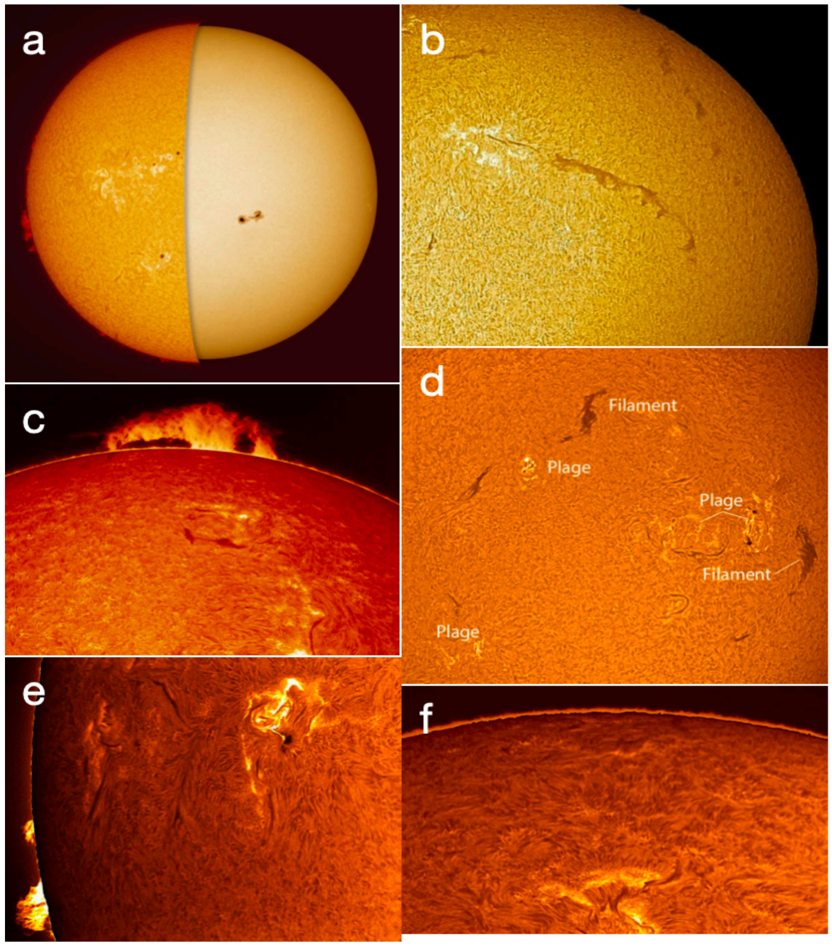

Figure 20: Hα observations of the Sun, showing: (a) composite image of the Sun in Hα (left) and white light (right), (b) a long filament, (c) a large quiescent prominence, (d) plages and filaments, (e) a C-class solar flare (upper right) and prominences (lower left), and (f) spicules.

the light through the interferometer twice, to capture the Hα line. This method significantly reduces stray light and improves the contrast and clarity of the spectral lines.

Hydrogen I Lyman Alpha (1216 Å) The H I Lyman alpha (hereafter referred to as Lyα) line is the strongest line among the ultraviolet chromospheric emission lines. The FWHM of the line core is very broad ($\sim$ 1 Å) due to Stark and Doppler broadening and the high optical thickness. The line center probably forms in the low transition region ($\sim$ 40000 K), while the wings form in the chromosphere ($\sim$ 6000 K) by partial redistribution of the core emission (see Figure 12). Thus, the Lyα line plays a critical role in the radiation transport in the low transition region and chromosphere (*Vourlidas et al. 2010* [59]). The emission of the Lyα line is essentially contributed by two components (*Gabriel 1971* [18]): (1) the resonance scattering of chromospheric Lyα protons by the small fraction of residual neutral hydrogen in the corona; (2) the excitation of residual neutral hydrogen by collisions with free electrons. Up to now, the Lyα band has been adopted by many spacecrafts as a means of observing the Sun. For example, the Solar Orbiter spacecraft, which was launched in 2020 by ESA, carries a dual-waveband coronagraph called Metis that will observe the extended corona in both Lyα and white light (WL) (*Antonucci et al. 2020* [3]). As the first space-borne solar observatory of China, the Advanced Space-based Solar Observatory (ASO-S; *Gan et al. 2019* [19]) is also equipped with the Lyman-alpha Solar Telescope (LST; *Li et al. 2019* [31]) that will image the Sun from the disk center up to 2.5 R_S using both Lyα and WL bands.

Lyα is very optically thick and results in both absorption and emission depending on the plasma environment. This interplay occurs at the height where the plasma starts to be dominated by the

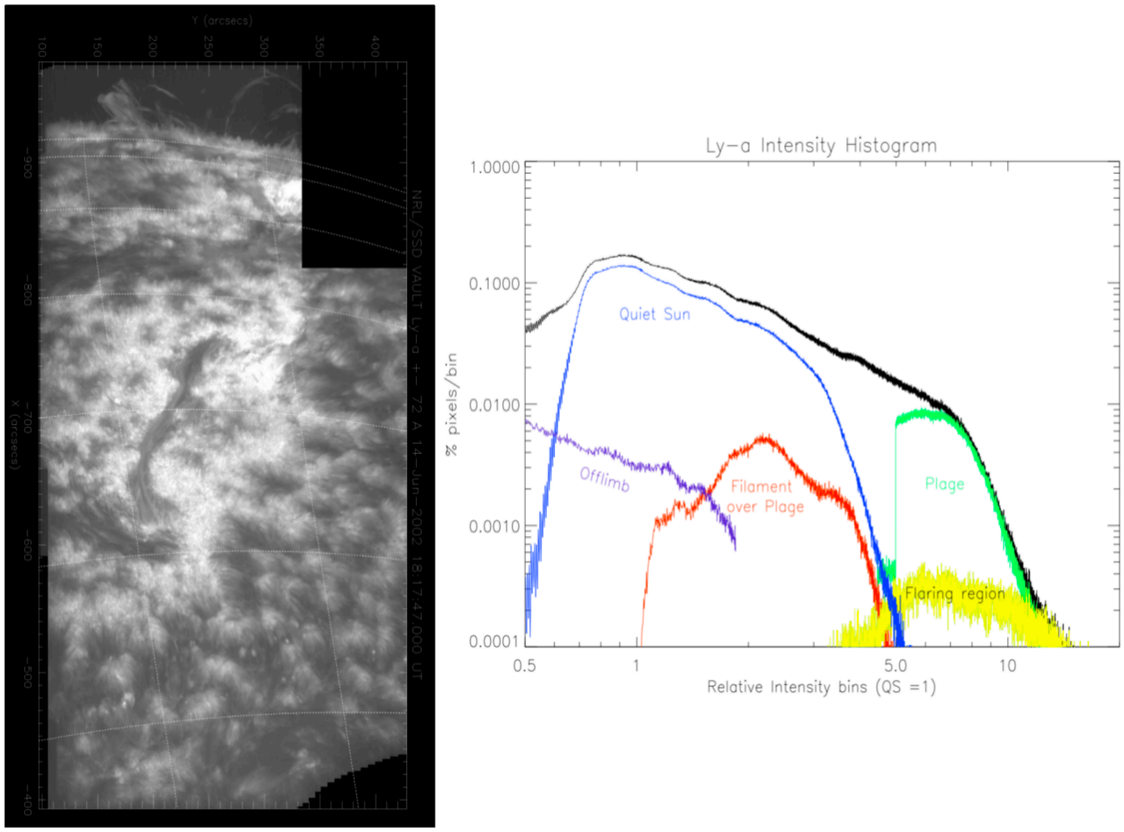

Figure 21: Left: The total solar field of view Right: Lyα emission histogram (black line). Different colors indicate partial histograms from subregions. Cover area for each type (integral over the histogram curve) is: Total (black line): 100%, Quiet Sun: 61%, Plage:13%, Filament: 2%, Flaring region: 1%, Offlimb: 1%, Rest: 23%. Figure directly adopted from *Vourlidas et al. (2010)* [59].

magnetic field, creating a wide range of intensities. On the other hand, the strength and variability of the Lyα emission have important effects on Earth because it affects the chemistry of the mesosphere as well as the climate on longer time scales. To fully understand the Lyα irradiance, the contributions of various solar resources should be examined at first (*Vourlidas et al. 2010* [59]). Figure 21 shows the observation by the Very high Angular resolution ULtraviolet Telescope (VAULT; left), and the corresponding intensity histograms for each domains relative to the overall histogram derived from the observations showing in the left (*Vourlidas et al. 2010* [59]). The *Quiet Sun (blue)* covers 61 % of the pixels with normalized intensity varying from 0.5 to 5, indicating high optical thickness and plasma structuring. This region also includes localized brightenings possibly caused by explosive events. The *Plage (green)* region in the central part of the FOV of VAULT covers 13 % of the pixels, with typical normalized intensities from 5 to 15. Since the only other contribution at these regions comes from a flare at the north edge of the image, the total solar Ly irradiance can be approximated using the Quiet Sun level adding a multiplying factor $\sim$7 for the percentage of the disc corresponding to plages (which could be obtained from other lines like Ca). *Filaments* cover the plage reduced observed intensity to Quiet Sun values, covering 22 % of the plage area. This indicates that filaments are sufficiently opaque. *Limb structures*, including spicules and large loops reaching heights of $60''$, show Quiet Sun levels of emission down to the detection threshold of 0.5. It is likely that these structures are nearly optically thin, implying temperature $\gtrsim$ 30,000 K.

2.2.3 Corona

The *Corona* is the outermost layer of the Sun's atmosphere, extending around 10 solar radii from the Sun's surface. It can be observed as a white halo surrounding the Sun during a solar eclipse. The corona is characterized by its extremely high temperature, ranging from 1 to 3 million K, which results in the emission of X-rays and ultraviolet radiation. The corona is composed of highly ionized gases, structured by the Sun's magnetic field into loops, streamers, and plumes.

One of the most prominent features of the corona is its dynamic and complex nature, with intense changes driven by solar activities. *Coronal mass ejections (CMEs)* are large expulsions of plasma and magnetic field from the Sun's corona, which could have profound effects on space weather. The corona also continuously emits the *solar wind*, a stream of charged particles that flows outward from the Sun, permeating the solar system and interacting with the Earth's magnetosphere. Studying the corona is crucial for understanding solar-terrestrial interactions and predicting space weather phenomena. The *Parker Solar Probe* and the *Solar Orbiter* are two recent missions that aim to study the corona up close and provide new insights into the Sun's outer atmosphere. Because of the high temperature of the coronal gas, its primary emission is in the ultraviolet (UV) and X-ray. In this section, we will discuss some typical wavelengths that are often used to observe the corona, and explain their importance in research.

Fe IX 171 Å Line Fe IX emits one of the strongest lines in the spectrum of solar corona that stands out at 171 Å, relatively isolated from a crowd of nearby Fe VIII and Fe X lines. The very high brightness of this line, its insensitivity to electron density, and its isolation in the spectrum make it one of the most promising choices for narrowband imagers to observe the corona at high resolution and high cadence. These imagers include: the Atmospheric Imaging Assembly (AIA; *Lemen et al. 2012* [30]) onboard the Solar Dynamics Observatory (SDO; *Pesnell et al. 2012* [41]), the Extreme Ultraviolet Imager (EUI; *Rochus et al. 2020* [44]) onboard the Solar Orbiter (SO; *Muller et al. 2020* [38]), and so on.

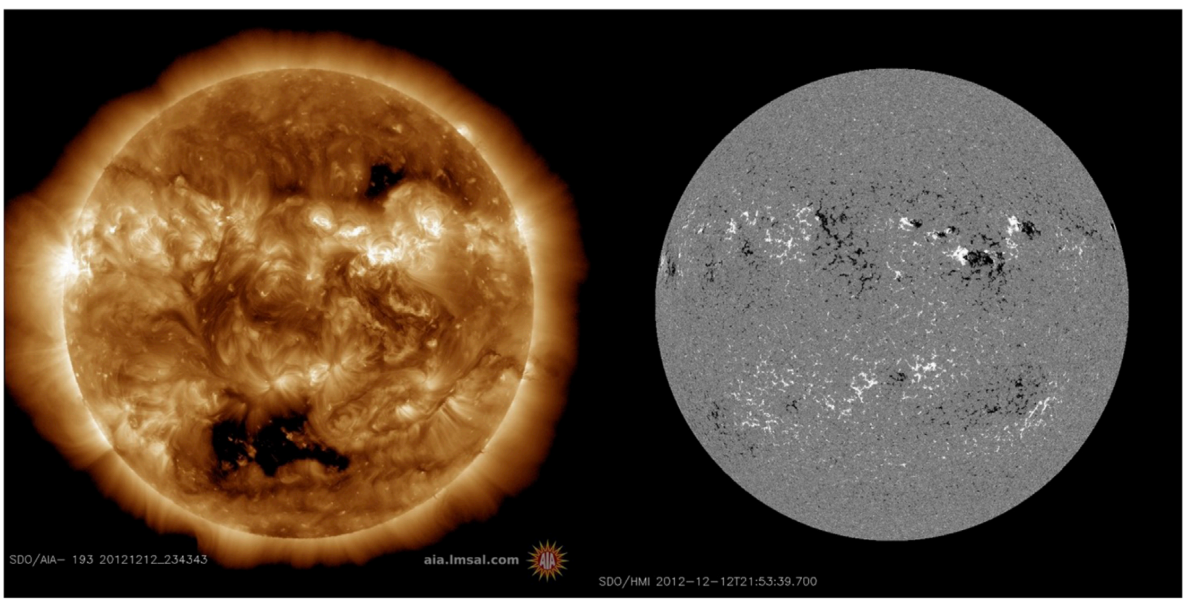

Figure 22: Observation the Sun on 12 December 2012, with AIA/SDO (left) showing the magnetically-dominated coronal EUV emissions, and HMI/SDO (right) showing the solar surface magnetic field.

Figure 22 shows an example of AIA/SDO measurements at 171 Å and HMI/SDO measurements of the solar surface magnetic field. The bright regions (hot emmision) in the AIA images correspond to the strong magnetic field regions in the HMI images, which are often referred to as active regions. The dark regions are called coronal holes, which are the least active regions of the Sun. Loops are bright, arched structures connecting regions of opposite magnetic polarity. They are often seen in active regions. Coronal holes are associated with rapidly expanding magnetic fields and the acceleration of high-speed solar wind. During solar minima, coronal holes are predominantly found near the Sun's polar regions. These polar coronal holes are large and stable, often persisting for many months. During solar maximum, coronal holes can appear at all latitudes, including the equatorial regions (*McComas et al. 2003* [36]). The importance of studying coronal holes lies in at least three reasons (*Cranmer 2009* [14]): 1. The extended corona and the solar wind that originate from the coronal holes tends to exist in an *ambient time-steady* state. Coronal holes thus serve as a perfect starting point for theoretically modeling because it is often advantageous to begin with simpler regions before attempting to model more complex regions. 2. Coronal hole plasma has the lowest density, which makes it an optimal testbed for researches about *collisionless kinetic process*. 3. Coronal holes and their asssociated high-speed solar wind contribute to a fraction of major geomagnetic storms at 1 AU. The hair-like structures along the solar limb, if seen in the polar regions, are called plumes. In the low-latitude regions, they might be spicules or loops. Spicules are dynamic, jet-like structures that originate in the chromosphere and extend into the corona.

X-ray X-ray astronomy began in 1949 by US scientists who launched a V-2 rocket to an altitude of 200 km carrying an X-ray detector to observe the Sun (*Burnight & Robert, 1949* [9]). Note that astronomical X-ray observations need to be performed from high latitude rockets and satellites because the Earth's atmosphere absorbs X-rays. The corona emits X-ray due to its high temperature of a few million K, which is also the strongest X-ray source all over the sky. X-ray in astronomy is often divided into soft X-ray (SXR) and hard X-ray (HXR). SXR ranges from 0.1 nm to 10 nm, corresponding to energy of 0.1 to 10 keV, whereas HXR ranges from 0.001 nm to 0.1 nm, corresponding to energy of 10 to 100 keV. The first X-ray spectrum of the Sun was recorded with a Bragg crystal spectrometer on board a sounding rocket (*Blake et al. 1965* [8]). The X-ray line spectrum between 1.3 and 2.5 nm showed many emission lines.

SXR observations are recognized as the best way to study the solar corona, as they are largely free from the contaminating emission from other temperature regimes. They also provide a reliable method for seeing the corona on the disk with the troublesome line-of-sight integration effects eliminated (*Golub et al. 1990* [21]). Figure 23 shows comparison of the active-region loops seen in X-rays with the regions visible in Ha at the footpoints of the loops, which would serve as an example of X-ray observations of the Sun. These observations are strong evidence of the view proposed by *Rosner et al. (1978)* [45] that loops terminate in the penumbra of sunspots. This indicates that the transfer of turbulent energy from the photosphere to the corona would be inhibited in spot umbrae due to the strong magnetic field, leading to reduced coronal heating.

A large variety of imaging, spectrograph, and detector schemes are employed in astronomical X-ray observations (*Ramsey et al. 1994* [43]). One method that is usually used to imaging the Sun in X-ray is the *grazing incidence optics*, which focus the FOV onto a small area similar to optics in the visible light. This method results in a dramatic increase in sensitivity and allows the usage of small, high-performance detectors. Another commonly used method is the *normal incidence optics*, where the collective area is large. Normal incidence optics describes optics where the beam is almost normal to the optical surfaces. Generally, normal incidence optics reach high spatial resolution with modest telescope diameters. Spectrometers measure the X-ray intensity as a function of wavelength, which can be used to determine the temperature, density, and velocity of the emitting plasma. There are two main spectrometer types used in X-ray astronomy: *Bragg crystal* and *grating spectrometers*. Bragg crystal spectrometers work by utilizing the interference of X-rays reflected off a crystal lattice, where the periodic arrangement of atoms causes different wavelengths to reflect at specific angles (Bragg reflection). Similarly, grating spectrometers use a periodic change in reflectivity or transmission to achieve wavelength-dependent reflection angles. When an X-ray beam interacts with a Bragg crystal or grating, various wavelengths are reflected at different angles. A detector then measures the intensity based on these reflection angles, thereby determining the wavelengths. For detectors, the general principle lies in the interaction of X-rays with the detector material, which results in free electric charges that are measured. In this case, gas-filled detectors and charge-coupled devices (CCDs) are the most commonly used detectors in X-ray astronomy.

3 Some Existing Solar Observatories and Their Performance

In this chapter, I will introduce three solar observatories: the New Vacuum Solar Telescope (NVST; *Liu et al. 2014* [34]), the GREGOR Solar Telescope, and the Solar Dynamics Observatory (SDO; *Pesnell et al. 2012* [41]), representing domestic ground-based solar telescopes, international ground-based solar telescopes, and space-based solar telescopes, respectively.

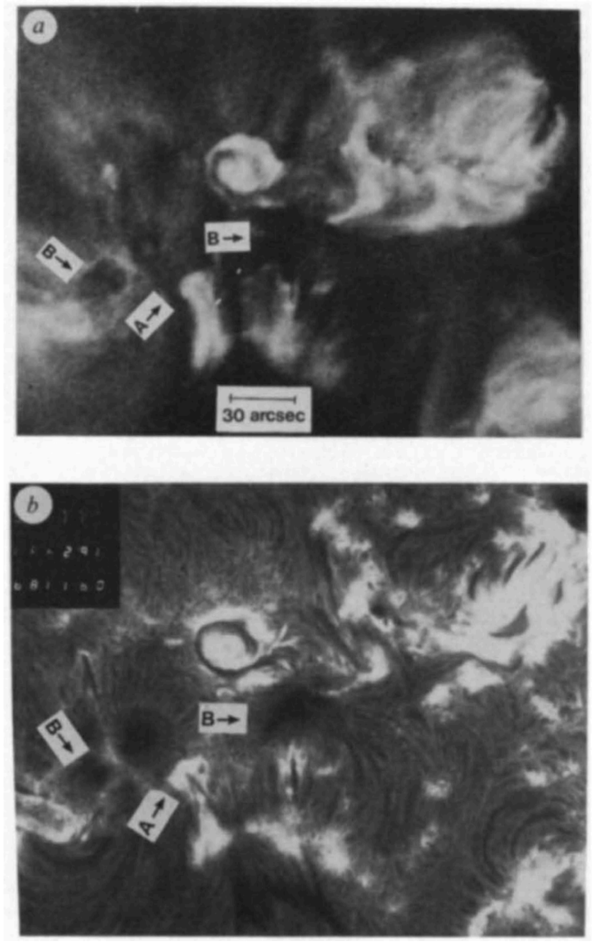

Figure 23: (a). Amplification of a 60-s exposure of the corona taken by the Normal Incidence X-ray Telescope (NIXT) in SXR at 16:38 UT on 11 September 1989. Arrow labelled A indicates footpoint of a loop, arrows labelled B point to dark coronal regions located above sunspots. (b). Hα image of the same region taken at 16:24 UT. Arrow labelled A indicates penumbral brightenings associated with the footpoint of coronal loops; arrows labelled B indicate sunspots. Figure directly adopted from *Golub et al. (1990)* [21].

3.1 New Vacuum Solar Telescope (NVST)

3.1.1 Introduction of NVST

The New Vacuum Solar Telescope (NVST; *Liu et al. 2014* [34]) is a one-meter vacuum solar telescope that aims at resolving fine structures on the Sun. The scientific goal of NVST are high-resolution imaging and spectral observations, including measurements of the magnetic field. The Chinese solar research community proposed this project for this solar cycle. NVST serves as the primary observing facility of the Fuxian Solar Observatory (FSO), which locates at the northeast side of Fuxian Lake (See Figrue 24). The Fuxian lake is famous for its significant stable atmosphere and good seeing conditions, which are ideal for solar observations.

NVST was originally proposed as a ground-based large scale spectrometer associated with the Chinese one-meter Space Solar Telescope, thus the early science investigations of NVST focused on spectral observations of the Sun. The original working mode of NVST was multi-band spectral observations, including measurements of the Stokes parameter of the solar lines that are sensitive to magnetic fields. However, due to the good seeing, the NVST team decided to expand their goals to cover more scientific topics. Now, the scientific goals of NVST include: observing the Sun with high spatial and spectral resolution in the wavelength range of 300 to 2500 nm, detecting small-scale magnetic structures and their coupling with the plasma, investigating the energy transfer, storage and release in the solar at-

Figure 24: The building (left) and the telescope (right) itself.

mosphere (*Liu et al. 2014* [34]). NVST will contribute to the understanding of key questions in solar physics, including the heating of the corona, the triggering of solar eruptions, and the evolution of solar activities, etc. As the primary observing facility used by the Chinese solar research community, NVST is also capable of undertaking more goals related to science and technology, including necessary experiments for key technologies of developing next generation solar observers.

3.1.2 Structure of NVST

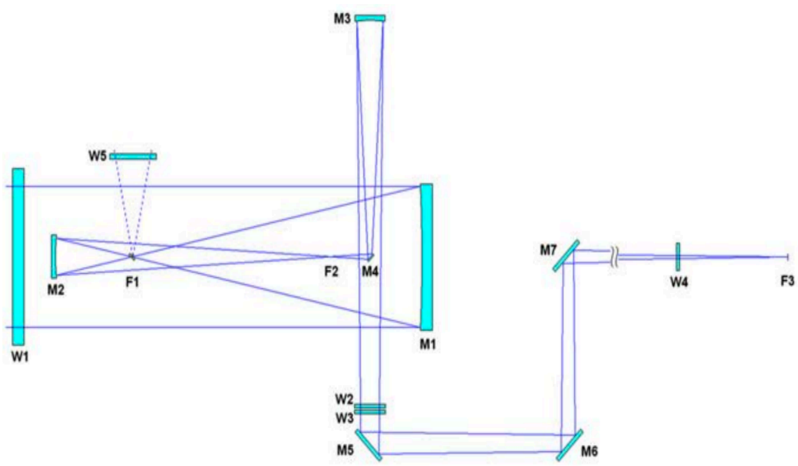

Figure 25: The optical system of NVST. Figure directly adopted from *Liu et al. 2014* [34].

The optical system of NVST is shown in Figure 25. An optical window (W1) with a diameter of 1.2 m is positioned at the top of the vacuum tube to maintain the air pressure inside the tube below 70 Pa. Following W1, the optical system comprises a modified Gregorian configuration with an effective focal length of 45 meters. The primary mirror (M1), the parabolic mirror, has a clear aperture of 985 mm. At the primary focus (F1), there is a 3.0 field diaphragm (heat stop) to prevent excess energy from entering the system. Unwanted light is directed out of the system through another vacuum window (W5) located on the side of the vacuum tube. The secondary mirror (M2) converges the light into F/9 beam and focuses it at the secondary focus (F2), where the polarization calibration unit is installed.

Clear Aperture	985 mm
Field of view	3'
Focal Length at F3	45 m
Spectral range	300 - 2500 nm
Tracking accuracy	< 0.3 "
Pointing accuracy	< 5 "

Table 1: Key parameters of NVST optical system (*Liu et al. 2014* [34]).

A small flat mirror reflects the light horizontally. The third imaging mirror (M3) further converges the light to the third focus (F3). After F3, three flat reflectors (M5-M7) direct the light. M3 also serves as the focusing mirror for the whole system. Table 1 shows the key parameters of the optical system. NVST comprises an adaptive optics (AO) system, which is a low order system with 37 actuators placed before other instruments but before F3 (*Liu et al. 2014* [34]).

3.1.3 Instrumentation of NVST

Magnetic field measurement The basic approach of measuring a magnetic field with NVST is to measure the polarization by using the Zeeman effect. The telescope's structure before M4 is designed to be symmetrical both optically and mechanically to minimize extra instrument polariozation. For instance, the spiders supporting the secondary mirror and the heat stop are cross-shaped rather than the simpler and easier-to-adjust tripod shape. Originally, the polarization analyzer (PA) for NVST was designed as a fast modulation system utilizing liquid crystal wave plates (*Xu et al. 2006* [61]). These plates were initially proposed to be installed close to F2 to enable high-precision solar polarization measurements. However, the PA system did not fit within the allowed space for NVST's optical system, leading to its replacement with a rotating modulation system using classical wave plates. The current PA is positioned before the spectrometer slit, while the calibration unit remains near F2. The entire polarization system is achromatic around both 5000 and 10000 Å. In combination with the spectrometers, the system can accurately measure Stokes parameters in both optical and near-infrared bands, such as 5324 and 10830 Å. The PA and calibration unit can be moved in or out of the optical path simultaneously or separately, depending on the observing modes. Once the ongoing installation and calibration are completed, the expected accuracy of polarization measurements is anticipated to be better than 5×10^{-3}.

Imaging system The primary scientific objective of NVST is to observe fine structures in both the photosphere and the chromosphere. The imaging system is installed on a rotating platform with a diameter of 6 meters. This system features a multi-channel high-resolution imaging setup, comprising one channel for the chromosphere and two channels for the photosphere. The chromosphere is observed using the Hα band (6563 Å), while the photosphere is observed using the TiO band (7058 Å) and the G-band (4300 Å). The Hα filter is a tunable Lyot filter with a bandwidth of 0.25 Å. It can scan spectra in the ± 5 Årange with a step size of 0.1 Å. All channels, connected to optical splitters, can synchronously observe and record images, allowing simultaneous observation of fine structures and their evolution in both the photosphere and the chromosphere.

Figure 26 shows high resolution observations of the photosphere magnetic field and the chromosphere. The observation includes: photospheric bright points, fine structures of solar activities, microsolar activities such as microfilaments and their evolution, and similar phenomena. All these features are important to modern solar physics and need high angular resolution near the diffraction limit of NVST.

Spectrometers Measuring spectra from the solar atmosphere is another key objective of NVST, as it is the primary method for detecting magnetic and velocity fields in the solar atmosphere. In addition to traditional scientific goals, NVST can detect small-scale structures in the photosphere and chromosphere using spectrometers in conjunction with the adaptive optics (AO) system. These small structures include bright points, dynamic features with plasma inside a flux tube, and the fine structures of quiescent filaments, among others.

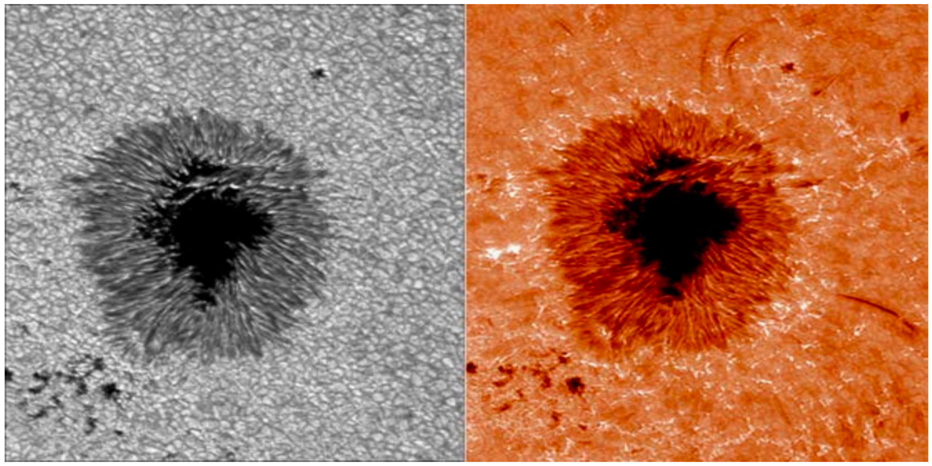

Figure 26: High resolution reconstructed images of the photosphere (7058 Å, left) and the chromosphere (Hα-0.8 Å, right) showing AR 11598. Figure directly adopted from *Liu et al. 2014* [34].

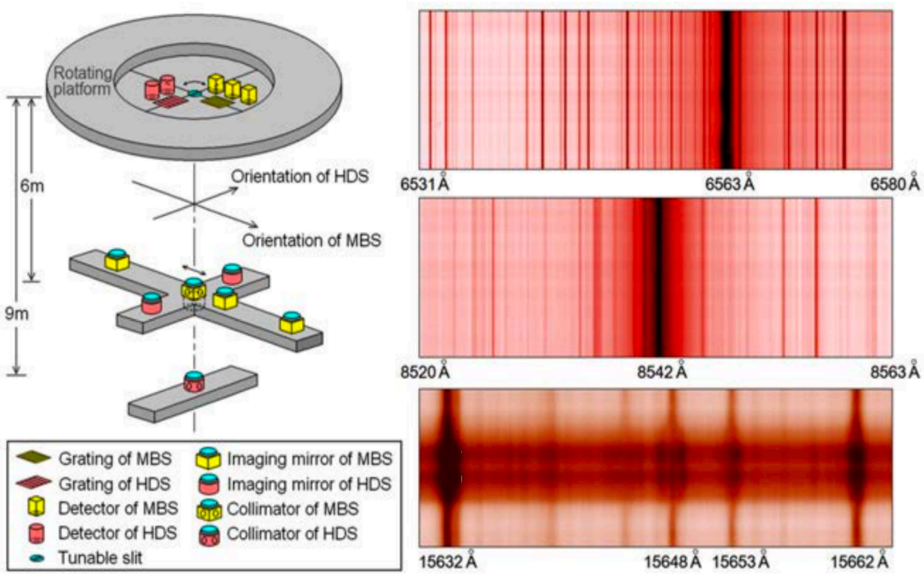

Figure 27: 3-D skech of the spectrometer (left) and some observation results (right). Figure directly adopted from *Liu et al. 2014* [34].

Spectrometer	MBS	HDS
Grating (mm^{-1})	1200 (blazed grating)	316 (echelle grating)
Blazed angle	36.8	63
Focal length of imaging mirrors (m)	6	6
Focal length of collimating mirror (m)	6	9
Effectove size of grating	156 $\times$ 130	334 $\times$ 196
Primary lines (Å)	5324, 8542, 6563	10 830, 15 648
Dispersion (mm / Å)	0.75 at 6563 Å	0.77 at 15648 Å
Resolution ($\Delta\lambda/\lambda$)	130000	300000 - 400000
Spectral range (Å)	> 50	> 20

Table 2: Key parameters of the NVST spectrometer. Table directly adopted from *Liu et al. 2014* [34].

The spectrometers integrated into the NVST include a multi-band spectrometer (MBS) and a high-dispersion spectrometer (HDS). These spectrometers are mounted on a vertical hanging bracket located just below the rotating platform, which serves as a large image derotator. The spectrometers share an adjustable slit positioned at the center of the rotating platform, with its width and orientation customizable to suit different spectrometers and scientific objectives. Before reaching the slit, approximately 10% of the photons are redirected to the imaging system to display the image and the slit's position. The spectrometers are oriented perpendicularly to each other (see the left panel of Figure 27) and share the same slit. Switching between the MBS and HDS involves rotating the slit and removing the collimating mirror used by the MBS. This switch must be completed before observations begin, as the two spectrometers cannot operate simultaneously.

The gratings used by the two spectrometers are different: MBS uses a blazed grating, while HDS uses an echelle grating. Both gratings are mounted on the reverse side of the platform, facing the collimating mirrors (see Figure 27). Imaging and collimating mirrors are positioned on vertical hanging brackets. The detectors, located face down on the central part of the rotating platform, record the spectrograms focused by the imaging mirrors. The substantial space occupied by the spectrometers helps to minimize scattered light. Table 2 provides the key parameters of MBS and HDS, and the right panel of Figure 27 shows some preliminary observational results from the two spectrometers. These results have been calibrated to correct obvious aberrations and remove visible interference fringes.

3.2 GREGOR Solar Telescope

3.2.1 Introduction of GREGOR

The 1.5-meter GREGOR telescope offers new insights into small-scale solar magnetisim (*Schmidt et al. 2012* [51]). Its initial instruments include the Gregor Fabry-Pérot Interferometer (GFPI), a visible wavelength filter spectro-polarimeter, the GREGOR Infrared Spectrograph (GRIS), and the Broad-Band Imager (BBI). The GFPI and GRIS have already shown excellent performance at the Vacuum Tower Telescope. As Europe's largest solar telescope and the third largest globally, GREGOR features an all-reflective Gregory design, providing extensive wavelength coverage from the near UV to at least 5 μm. It has 150-arcsec diameter field of view and is equipped with a high-order adaptive optics system, which includes a 10 cm subaperture and a deformable mirror with 256 actuators. GREGOR's primary scientific goals focus on solar magnetism, allowing for detailed measurement of magnetic flux emergence and disappearance at the solar surface on spatial scales below 100 km. Its spectro-polarimetric capabilities enable the study of interactions between plasma flows, various waves, and the magnetic field, enhancing our understanding of the heating processes in the chromosphere and outer solar atmosphere. Observing surface magnetic fields at very small spatial scales will also contribute to our knowledge of solar brightness variability.

GREGOR is located at the Observatorio del Teide on Tenerife, Spain, which is one of the best sites for solar observations in Europe. Together with the neighboring Vacuum Tower Telescope (VTT) and the 90 cm THEMIS, GREGOR forms the world's most powerful set of solar telescopes at a single site. Figure 1 shows an aerial view of the Observatorio del Teide (OT) with the three large solar telescopes aligned along the ridge. In the lower right corner of the image is THEMIS, followed by VTT and GREGOR.

3.2.2 Scientific Objectives of GREGOR

The magnetic field plays a dominant role in the solar atmosphere, influencing the dynamics and energetics of the plasma. Many important questions related to solar magnetism remain unanswered, such as the mechanism that generates the solar cycles and the triggering of solar activities. The good coverage observation from space-based telescopes like SDO provide a wealth of data on solar magnetism on spatial scales larger than 1 arcsec. These scales are important for understanding the overall behavior of the magnetic field. They offer valuable information about the movement of the magnetic field relative to the plasma and provide insights into the dynamics of active regions as a whole. However, a large fraction of the magnetic flux on the Sun is located at spatial scales below 1 arcsec, and at these scales, time scales below 1 minute are important. Observations of the solar magnetism at high spatial and temporal resolution are therefore of high importance for the comprehension of the solar magnetism. Large-aperture telescopes like GREGOR are thus needed for at least two reasons (*Schmidt et al. 2012* [51]): (1) to provide sufficient photon flux for a given area on the Sun to allow

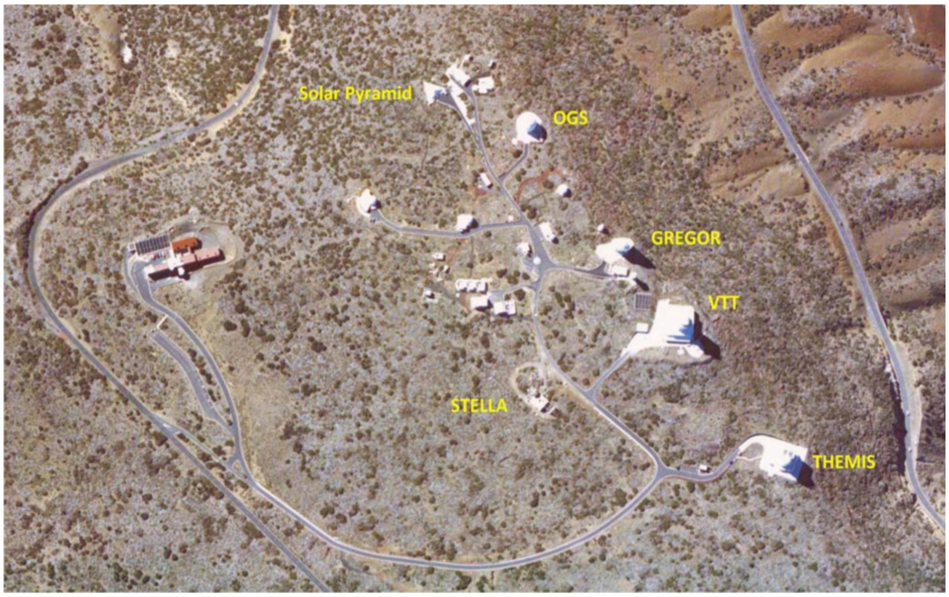

Figure 28: Solar telescopes on Tenerife, including THEMIS, VTT, and GREGOR. Above GREGOR lies the Optical Ground Station (OGS) of ESA. The STELLA installation is located just opposite of the access road to VVT. Figure directly adopted from *Schmidt et al. (2012)* [51].

for high-precision measurements of the magnetic field; (2) to achieve high spatial resolution down to a few tens of kilometers to spatially resolve small magnetic flux concentrations.

The scientific objectives of GREGOR can be briefly summarized as following (*Schmidt et al. 2012* [51]):

1. *To study the interaction between convection and the magnetic field in the photosphere.*

   In the quiet solar photosphere, key themes include the emergence and dissipation of magnetic flux, as well as the interaction of small-scale magnetic flux concentrations with the surface's convective motion, known as granulation. For a proper comprehension of this phenomenon, observations with highest resolution are needed.

2. *To understand the structure of sunspots.*

   This topic includes the structure and dynamics of sunspots with their complex flow and magnetic patters. Structures such as umbra dots, Evershed flow, and dark lanes still pose challenges to our understanding of sunspots. The high spatial resolution of GREGOR will allow for detailed studies of these structures.

3. *To uncover the role of solar magnetism in causing solar variability.*

   It is well known that the solar activity follows a 11-year cycle. At the maximum of a cycle, the solar constant is roughly 0.1 % higher compared to this value at solar minimum (*Ohlich et al. 2006* [40]). The increase of the total brightness at solar maximum is caused by small-scale faculae with angular sizes on the order of $0.1''$. The total solar irradiace variations are also confirmed to be caused by the magnetic field at the solar surface (*Ball et al. 2012* [6]). Accurate measurements of the solar magnetism in this solar cycle is important to clarify this issue.

4. *To understand the enigmatic heating of the solar chromosphere.*

   The relative importance of magnetic field and acoustic waves for heating the chromosphere is still under debate. The short timescales of chromospheric dynamics are short, the weak magnetic field, and the low light level present an observational challenge that can only be addressed with a large-aperture solar telescope.

5. *To search for solar twins.*

Stellar statistics suggest that there are approximately one billion G2 stars in our galaxy, with about 3000 of these stars within a 250 light-year radius of the Sun. However, only a few solar twins have been identified spectroscopically so far. Night-time observations using GREGOR will conduct a large spectroscopic survey to investigate aspects such as the evolution of angular momentum in solar twins.

3.2.3 Structure of GREGOR

The optical design of GREGOR is shown in the left panel of Figure 29. GREGOR is a double Gregory system equipped with three imaging mirrors. Its primary mirror has a diameter of 1.5 meters and a focal length of 2.5 m, producing a 25 mm diameter image of the solar disk in the primary focal plane. This image carries a total power of approximately 2000 W and a flux density of about 6 MW/m^2. A water-cooled system is used at this location to deflect most of the sunlight out of the telescope, transmitting a circular field-of-view with a diameter of about 150 mm through a central hole. To reduce the heat load on the field stop, the reflecting surface is coated with protected silver to increase reflectivity and decrease absorption. The elliptical secondary mirror forms a secondary image near the intersection of the optical and elevation axes of the telescope, where the removable GREGOR Polarization Calibration Unit (GPU; *Hofmann et al. 2012* [23]) is installed. The beam then continues to the second elliptic mirror M3, which creates the final image at the F3 focus. The folding flat mirror M4 directs the light beam into the elevation axis, and additional flat folding mirrors guide the beam to the observing laboratory.

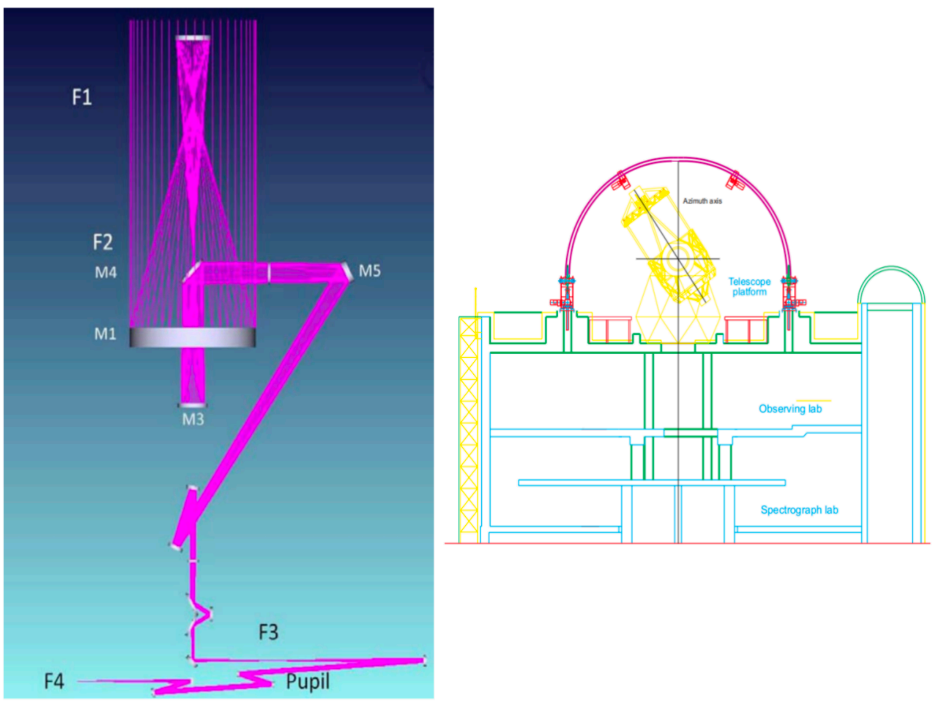

Figure 29: Left: Optical design of GREGOR. F1 - F3 denote focal planes of the telescope. The adaptive optics reimages F3 - F4. Right: Structure of the GREGOR building. Figure directly adopted from *Schmidt et al. 2012* [51].

The right panel of Figure 29 shows the structure of the GREGOR building, including the outline of the foldable dome (red). Thick green lines indicate the newly built concrete parts that are designed to increase the stiffness of the telescope platform Thin blue lines show the pre-existing infrastructure, which was used for the 45 cm Gregory Coudé telescope. Thin black lines indicate the azimuth axis, the optical axis of the telescope and the plane of the elevation axis. The spectrograph laboratory in Level 4 was modified by adding a wall to separate the spectrograph optics from the detector area.

3.2.4 Instrumentation of GREGOR

GRating Infrared Spectrograph (GRIS) The GRating Infrared Spectrograph (GRIS; *Collados et al. 2012* [13]) is a a Czerny-Turner spectrograph designed for high-resolution observations ($R = 300000 - 450000$) in the 1.0 to 1.8 μm wavelength range. This range covers spectral lines such as: Si I λ 1.079 μm, He I λ 1.083 μm, and Fe I λ 1.565 μm (g=3). GRIS can be paired with the Tenerife Infrared Polarimeter (TIP-2). It features a slit length of 70$''$ and an image scale of 0.135$''$/pixel. Scanning a 70$''$ $\times$ 70$''$ FOV takes less than 20 minutes while capturing full-Stokes spectra with a signal-to-noise ratio of 1000:1. The spectrograph achieves the telescope's diffraction limit at λ 1.565 nm. Multi-wavelength observations are facilitated by slit-jaw cameras and the GREGOR Fabry-Pérot Interferometer (GFPI). Figure 30 shows the light distribution system of GREGOR. As light enters the telescope from below, a beam splitter directs a small portion to the wavefront sensor of the AO system. A dichroic beam splitter then transmits the infrared light to GRIS and the slit jaw camera, while reflecting the visible light to the GFPI. The light is further split into the blue channel and the GPFI, with a 5:95 ratio between the broad and narrow channels of the GPFI.

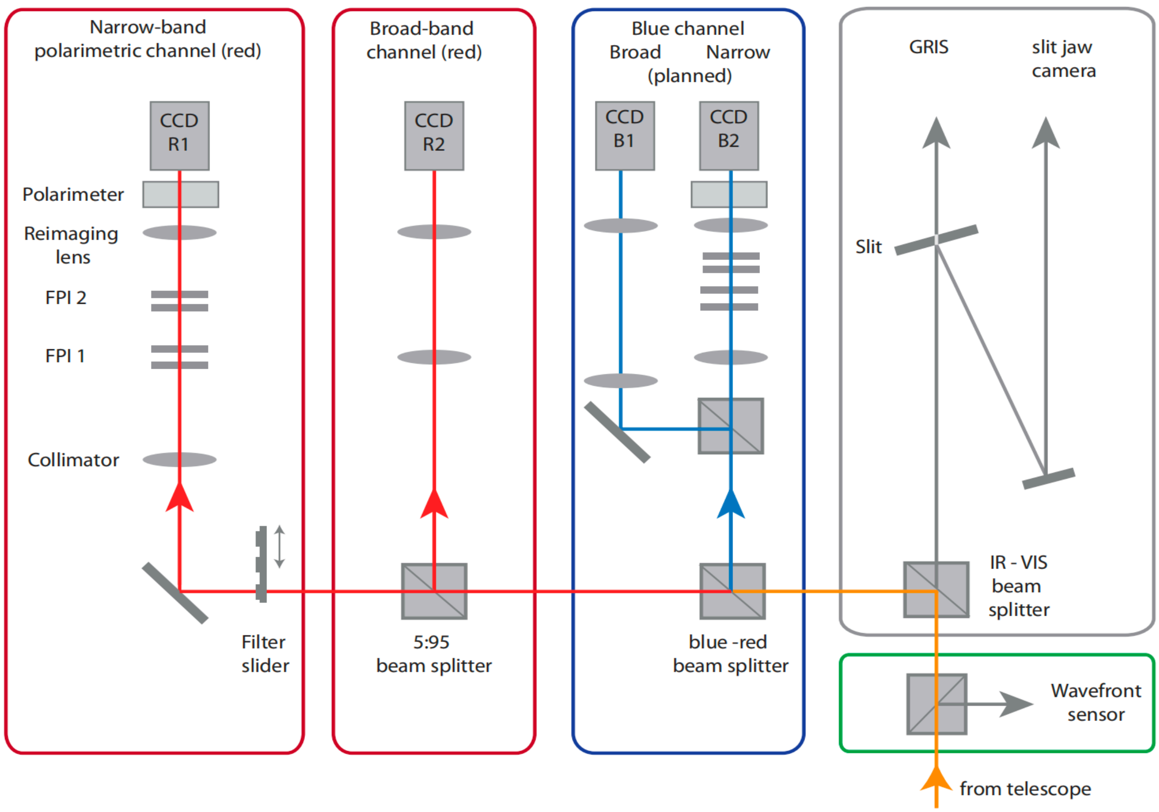

Figure 30: Scheme of the GREGOR Fabry-Pérot Interferometer (GFPI) and the light distribution system. Light from the telescope comes from below, entering a beam splitter. A small fraction of the light is sent to the wavefront sensor of the AO. Then a dichroic beam splitter transmits the infrared light to GRIS and the slit jaw camera, and reflects the visible wavelength band to the GPFI. A blue/red beam splitter deflects the blue part to the blue channel, and the remaining light are sent to the GPFI, where it is split with a ratio of 5:95 between the broad and narrow channel. Figure directly adopted from *Schmidt et al. 2012* [51].

GREGOR Fabry-Pérot Interferometer (GFPI) Fabry-Pérot interferometers can be configured in either a telecentric or collimated mounting. *Kneer & Hirzberger (2001)* [26] discussed the benefits and drawbacks of each and introduced initial concepts for an imaging spectrometer at the GREGOR solar telescope. The final optical design of the GFPI is detailed in *Puschmann et al. (2007)* [42]. This new instrument, based on the "Göttingen" Fabry-Pérot Interferometer, was upgraded in 2005 with new etalons, cameras, and software, and equipped with a polarimeter using ferroelectric liquid telescope in 2009. It offers a spectral resolution of about $R \approx 250000$ within the 530 - 860 nm wavelength range and can sequentially observe two spectral lines over a FOV of $52'' \times 40''$. A second Fabry-Pérot interferometer for the blue spectral region was proposed by *Denker (2010)* [15], who discussed the potential and challenges of imaging spectropolarimetry with new large-format, high-cadence camera systems.

Broad-Band Imager (BBI) The Broad-Band Imager (BBI; *Von der Lühe et al. 2012* [58]) is designed to capture filtergrams at visible wavelengths, down to 390 nm, with a field of view of $120'' \times 80''$. It achieves diffraction-limited imaging through post-facto reconstruction techniques. Sequences obtained with this instrument will be used to study the fine structure of photospheric granulation (*Steiner et al. 2010* [53]). The BBI features a PCO4000 camera with 4008×2672 pixels. A second channel of the BBI is utilized for Foucault tests to monitor the telescope's alignment and optical quality. The BBI was assembled by KIS, primarily using existing hardware from the VTT. The optical layout of BBI can be found in *Schmidt et al. (2012)* [51]. The BBI can capture bursts of short-exposure images for post-facto image reconstruction or use a phase-dilivery (PD) beam splitter to simultaneously record focused and defocused images for PD reconstruction.

3.3 Solar Dynamics Observatory (SDO)

3.3.1 Introduction of SDO

The *Solar Dynamics Observatory* (SDO; *Pesnell et al. 2012* [41]) aims to provide the data and scientific insights necessary to predict solar activity, from forecasting flares and coronal mass ejections (CMEs) on a daily basis to projecting solar activity levles in future solar cycles. By capturing high-resolution images that monitor the information and topology of magnetic fields formed within the Sun and extending through its outer atmosphere, the corona, SDO seeks to identify precursors for predicting flares and CMEs. One of the key insights SDO aims to deliver is understanding the topological configuration required to drive reconnection and reorganization in these stressed and built-up magnetic fields, which are the sources of energy release that trigger solar eruptive events.

Longer timescales require an understanding of how magnetic fields are transported, amplified, and dissipated within the Sun before being expelled from its interior. Within these broader timescales, another goal of SDO is to predict the emergence and location of active regions, the eruption and decay of magnetic fields, and the occurrence of various other phenomena associated with the solar magnetic field.

The SDO mission includes three scientific investigations: the *Atmospheric Imaging Assembly* (AIA; *Lemen et al. 2012* [30]), the *Extreme Ultraviolet Variability Experiment* (EVE; *Woods et al. 2012* [60]), and the *Helioseismic and Magnetic Imager* (HMI; *Scherrer et al. 2012* [50]). Two of the three instruments concentrate on the energy radiated in the extreme ultraviolet. As have been shown in Section 2, solar extreme ultraviolet (1 - 122 nm) photons are the primary cooling radiation of the solar corona and are also the dominant source of heating for the Earth's upper atmosphere. EUV photons can also break the bounds of atmosphereic atoms and molecules, generating a layer of ions that alters and sometimes disturbs the global communication system. SDO will also measure variations inside the Sun, providing the data needed to understand the internal motions that generate the magnetic field, and then the magnetic field as it emerges through the solar surface. These measurements allow for the study of the lifecycle of the solar magnetic field.

The SDO spacecraft is shown in Figure 31. A summary of the spacecraft is:

Satellite: Three-axis stabilized and fully redundant spacecraft.

Duration: Five years with a five-year extension option.

Mass: 3,000 kg: 300 kg for instruments, 1300 kg for spacecraft, 1400 kg for fuel.

Dimensions: The overall length of the spacecraft along the Sun-pointing axis is 4.7m, and each side is 2.2m. The span of the spacecraft is 6.1 m along the extended solar panels and 6.0 m along the deployed high-gain antennas.

Solar array: The 6.6 m^2 solar array produce 1.5 kW of power.

Orbit: Geo-syncronous orbit.

As the flagship mission that proposed by NASA for substantial enhancement of capabilities for solar physics, SDO is unique for the following reasons (*Pesnell et al. 2012* [41]):

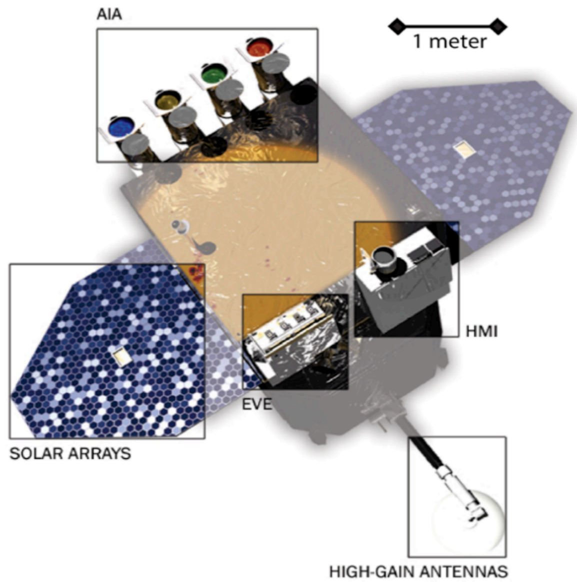

Figure 31: The SDO spacecraft with the instruments indicated. Figure directly adopted from *Pesnell et al. 2012* [41].

1. A continued high-rate of data production and the transmission of these data within the spacecraft.
2. The ability to transfer science data with a highly automated data pipeline which processes the data for immediate use by the science community.
3. Significant pointing accuracy and stability, which allows for registration of successive images.
4. The long (at least five years) mission life with high-duty cycle instruments.

3.3.2 Scientific Objectives of SDO

Scientific Questions
What mechanisms drive the quasi-periodic 11-year cycle of solar activity?
How is active region magnetic flux synthesized, concentrated, and dispersed?
How does magnetic reconnection on small scales reorganize the large-scale field topology and current systems, and how significant is it in heating the corona and accelerating the solar wind?
Where do the observed variations in the Sun's extreme ultraviolet spectral irradiance arise, and how do they relate to the magnetic-activity cycles?
What magnetic-field configurations lead to the coronal mass ejections, filament eruptions, and flares that produce energetic particles and radiation?
Can the structure and dynamics of the solar wind near Earth be determined from the magnetic-field configuration and atmospheric structure near the solar surface?
When will activity occur, and is it possible to make accurate and reliable forecasts of space weather and climate?

Table 3: The SDO Level 1 science requirements. Table directly adopted from *Pesnell et al. 2012* [41].

The Level 1 science goals of SDO is shown in Table 3. In order to address these questions, the instruments must be designed to meet the instrument science objectives listed in Table 4. The mea-

Measurements over a significant portion of solar cycle to capture the solar variations that exists on all time scales from seconds (solar eruptive events) to months (active region evolution, solar rotation) to years (solar cycle).
Measurements of the extreme ultraviolet spectral irradiance of the Sun at a rapid cadence.
Measurements of the Doppler shifts due to oscillation velocities over the entire visible disk.
Measurements of the longitudinal and vector magnetic field over the entire visible disk at a high resolution.
Images of the chromosphere and inner corona at several temperatures at a rapid cadence.

Table 4: SDO measurement objectives. Table directly adopted from *Pesnell et al. 2012* [41].

Invesitigation	Abbrev.	Returned Data
Helioseismic and Magnetic Imager	HMI	Full-disk Dopplergrams
		Full-disk line-of-sight magnetograms
		Full-disk vector magnetograms
Atmospheric Imaging Assembly	AIA	Rapid-cadence, full-disk EUV solar images
Extreme Ultraviolet Variability Experiment	EVE	Rapid-cadence EUV spectral irradiance

Table 5: The SDO science investigations. Table directly adopted from *Pesnell et al. 2012* [41].

surements will be presented in the format shown in Table 5. All questions are related to developing an understanding of the solar magnetic field and a predictive capability for solar activity.

3.3.3 Instrumentation of SDO

The scientific payload of SDO comprises three instrument suites. We present a brief summary of each in this section.

Helioseismic and Magnetic Imager (HMI) The Helioseismic and Magnetic Imager (HMI; *Scherrer et al. 2012* [50]) will map magnetic and velocity fields at the surface of the Sun. A key objective of the instrument is to decipher the physics of the solar magnetic dynamo. HMI measures the Doppler shift of the Fe I 6173 Å line to determine the photospheric surface velocity over the Sun's entire visible disk. It creates a full-disk photospheric surface velocity measurement (Dopplergram) every 45 seconds with a two-pixel resolution of $1''$, a noise level of approximately 25 m/s. HMI also uses Zeeman effect of the same line to measure the Stokes parameters required to create full-disk longitudinal magnetic-field measurements (LOS magnetogram) and full-disk vector photospheric magnetic-field measurements (vector magnetogram). The LOS magnetograms have a temporal resolution of 45 seconds, a two-pixel resolution of $1''$ resolution, a noise lvel of 17 G, and a dynamic range of ± 3 kG. The vector magnetograms have a temporal resolution of 720 seconds with a polarization accuracy of no less than 0.3 %.

The HMI investigation encompasses three primary LWS objectives (*Scherrer et al. 2012* [50]): (i) determine how and why the Sun varies; (ii) improve our understanding of how the Sun drives global change and space weather; and (iii) determine to what extent predictions of space weather and global chage can be made and to prototype predictive capabilities. We describe the broad goals in more details in the following content.

Convective-Zone Dynamics and the Solar Dynamo: Magnetic fields are generated by the fluid motions inside the Sun. Complex interactions between turbulent convection, rotation, large-scale flows, and magnetic field produce the solar activities in a quasi-periodic pattern. How are variations in the solar cycle related to the internal flows and magnetic fields? How is the differential rotation of the Sun formed and maintained? What is the structure of the meridional flow and how does it vary? What roles do the zonal-flow pattern and the variations of the rotation rate in the tachocline play in the solar dynamo? These questions are usually studied in zonal averages by global seismology, but the Sun is longitudinal structured. HMI will provide us with a new window to address these issues.

Links Between the Internal processes and Dynamics of the Corona and Heliosphere: Intrinsic connectivity between magnetic-field patters at different scales increases coronal structure complexity that leads to variability. For example, coronal mass ejections (CMEs) obviously interact with the global magnetic field, but many CMES are accompanied by flares, which are tought to be local phenomena. Model-based reconstruction of 3D magnetic fields is one efficient way to estimate the field from observations. More reliable MHD coronal models based on HMI high-cadence vector-field maps as boundary conditions will greatly improve our understanding of how the corona responds to evolving, non-potential active regions.

Precursors of Solar Disturbances for Space-Weather Forecasts: The number, strength, and timing of solar eruptive events that produce space weather are unpredicable at present. We can hardly answer the following questions: "Will the next solar cycle stronger than the current one?" "When and where will the next eruptive event occur?" Or "when will there be several successive quiet days?" These questions are important as we rely more and more on space-based technology. More knowledge about the internal motions, magnetic-flux transport and evolution, relations between active regions, UV irradiance, and solar-shape variations is needed to develop practical prediction tools. HMi observations will provide the data needed to understand the fundamental processes mentioned.

Atmospheric Imaging Assembly (AIA) The Atmospheric Imaging Assembly (AIA; *Lemen et al. 2012* [30]) is an array of four telescopes that observes the surface and atmosphere of the Sun. AIA was designed to obtain full-disk images of the solar atmosphere with a field of view of $\geq 40^{'}$ and a two-pixel reolution of $1.2^{''}$. The telescopes, combined with a series of filters, cover ten different wavelength bands that include 7 extreme ultraviolet (Fe XVIII 94 Å, Fe VIII, XXI 131 Å, Fe IX 171 Å, Fe XII, XXIV 193 Å, Fe XIV 211 Å, He II 304 Å, Fe XVI 335 Å), two ultraviolet (C IV near 1600 Å, nearby continuum 1700 Å), and one visible light band to reveal key aspects of solar activities. The temperature of the wavelengths ranges from 6000 K to 3×10^6 K. AIA uses multilayer coatings combined with foil filters to isolate the desired spectral bandpasses for each telescope.

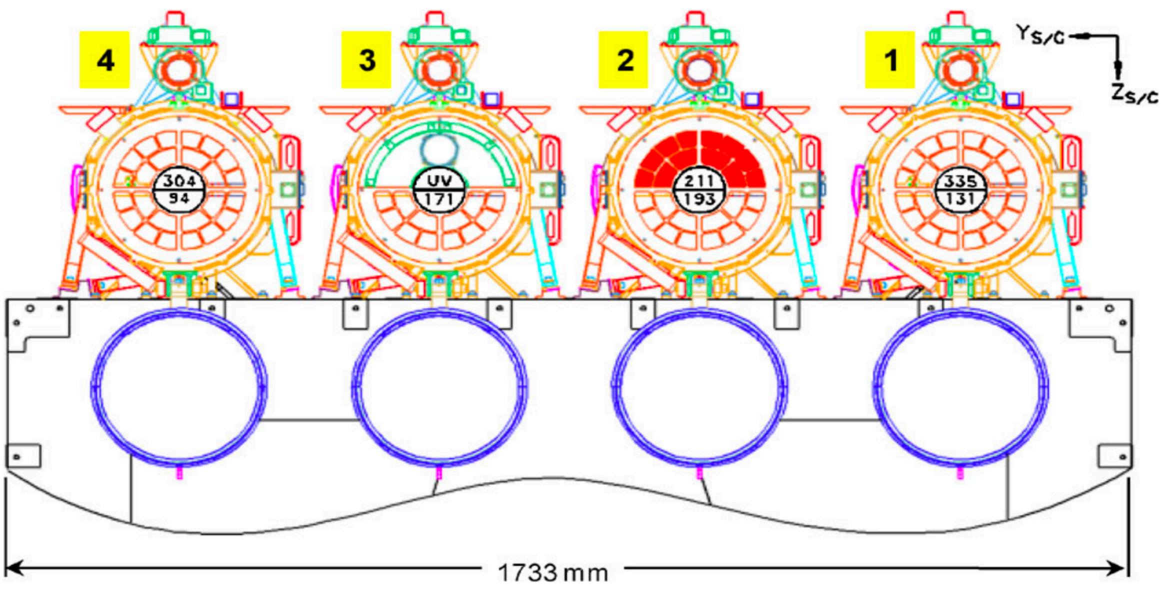

Figure 32: The layout of the wavelength channels in each of the four AIA telescopes. Telescope 2 has an aperture blade to select between wavelength channels. The other telescopes rely on filters in filter wheels to select between channels. The top half of telescope 3 contains a MgF_2 window with a coating centered at 1600 Å. Figure directly adopted from *Lemen et al. 2012* [30].

Figure 2 shows schematically the layout of the telescopes with respect to their wavelength band passes. The telescopes are designed as the following: (i) Four 20-cm, dual-channel, normal-incidence telescopes, which observe a 41 arcmin field of view in ten EUV and UV channels,with 0.6-arcsec pixels and 4096×4096 CCDs. Four of the EUV wavelength bands open new perspectives on the solar corona. The set of six EUV channels that observe ionized iron allow the construction of relatively narrow-band

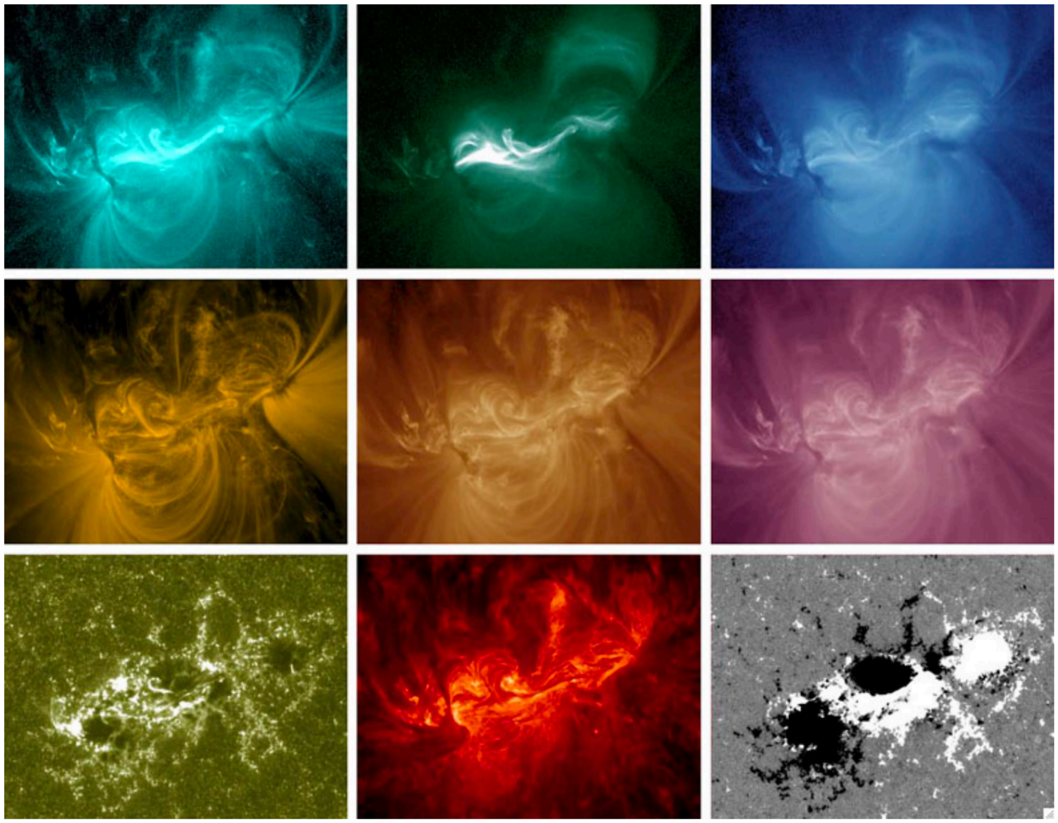

Figure 33: Images of an active region captured by AIA. From left to right: top row: 131-, 94-, and 335-Å images; middle row: 171-, 193-, and 211-Å images; bottom row: 1600-, 304-, and HMI line-of-sight magnetogram showing the same region.

temperature maps of the solar corona from below 1 MK to above 20 MK. (ii) Detectors with a full well of at least 150,000 electrons and a readout noise of less than 25 electrons. (iii) AIA is operated by a standard baseline observing program. AIA has the capability to adjust its observing program to changing solar conditions in order to implement observing programs that are optimized to meet the scientific requirements. With these telescopes, AIA provides the following essential capabilities; (i) A view of the entire corona at the best feasible resolutions compatible with SDO's constraints, offering coverage of the full thermal range of the corona; (ii) A high signal-to-noise ratio for two- to three-second exposures that reaches 100 in quiescent conditions for the low-temperature coronal-imaging channels, and duing flaring in the higher-temperature channels with a dynamic range up to 10000; (iii) Essentially uninterrupted viewing for months at a time at a temporal resolution of approximately 10 to 12 seconds, and can be adjusted to be faster when needed. These capabilities are necessary to cover the broad scientific objectives that focus on five core research themes: (i) Energy input, storage, and release: the 3D dynamic coronal structure, including reconnection and the effects of coronal currents; (ii) Coronal heating and irradiance: origins of the thermal structure and corlnal emission, to understand the basic properties of the solar coronal plasma and field, and the spatially-resolved input to solar spectral irradiance; (iii) Transients: sources of radiation and energetic particles; (iv) Connections to geospace: material and magnetic field output of the Sun; (v) Coronal seismology: a diagnostic to access sub-resolution coronal physics. These five themes guide the AIA science investigation.

An active region observed on 15 February 2011 is shown in Figure 33 for the seven EUV channels, the 1600-Åchannel, and an HMI LOS magnetogram. These images illustrate how the various instrument-response functions sample the temperature-dependent structure of the solar corona. We list the primary ion for each band pass, the characteristic emission temperatures, and the types of solar features that may be observed in Table 6.

Channel	Primaty Ion(s)	Region of atmosphere	Char. log(T)
4500-Å	continuum	photosphere	3.7
1700-Å	continuum	temperature minimum, photosphere	3.7
304-Å	He II	chromosphere, transition region	4.7
1600-Å	C IV	transition region, upper photosphere	5.0
171-Å	Fe IX	quiet corona, upper transition region	5.8
193-Å	Fe XII, XXIV	corona, hot flare plasma	6.2, 7.3
211-Å	Fe XIV	active-region corona	6.3
335-Å	Fe XVI	active-region corona	6.4
94-Å	Fe XVIII	flaring corona	6.8
131-Å	Fe VIII, XXI	transition region, flaring corona	5.6, 7.0

Table 6: The primary ions observed by AIA, with the features they observe and the characteristic temperatures included. Table directly adopted from *Lemen et al. 2012* [30].

Extreme Ultraviolet Variability Experiment (EVE) The Extreme Ultraviolet Variability Experiment (EVE; *Woods et al. 2012* [60]) measures fluctuatinos in the Sun's ultraviolet output. EVE will measure the solar spectral irradiance in the most variable and unpredicable part of the soalr spectrum from 0.1 to 105 nm as well as 121.6 nm. EVE includes three parts: MEGS, ESP, and SAM. MEGS combines grating spectrometers with two CCDs to create images of the spectral irradiance in various wavelength ranges. These individual sections are then combined to give the spectrum between 6.5 to 105 nm at 0.1 nm spectral resolution. ESP is a series of radiometers placed behind a transmission grating that measures the irradiance in several wavelength bands (0.1 - 5.9, 17.2 - 20.6, 23.1 - 27.6, 28.0 - 31.6, and 34.0 - 38.1 nm). SAM is a pinole camera, together with the MEGS-A CCD, measures individual X-ray photons in the wavelength range 0.1 - 7 nm.

References

[1] GK Aimanova and RA Gulyaev. Distribution of neutral sodium and velocity of nonthermal motions in the lower chromosphere based on eclipse observations of the resonance doublet d1-d2. *Soviet Astronomy, Vol. 20, p. 201*, 20:201, 1976.

[2] Ernest Alsina Ballester, Luca Belluzzi, and Javier Trujillo Bueno. Solving the paradox of the solar sodium d 1 line polarization. *Physical Review Letters*, 127(8):081101, 2021.

[3] Ester Antonucci, Marco Romoli, Vincenzo Andretta, Silvano Fineschi, Petr Heinzel, J Daniel Moses, Giampiero Naletto, Gianalfredo Nicolini, Daniele Spadaro, Luca Teriaca, et al. Metis: the solar orbiter visible light and ultraviolet coronal imager. *Astronomy & Astrophysics*, 642:A10, 2020.

[4] R Grant Athay and Richard C Canfield. Computed profiles for solar mg b-and na d-lines. *Astrophysical Journal, vol. 156, p. 695*, 156:695, 1969.

[5] LH Auer, JN Heasley, and LL House. The determination of vector magnetic fields from stokes profiles. *Solar Physics*, 55:47–61, 1977.

[6] William T Ball, Yvonne C Unruh, Natalie A Krivova, Sami Solanki, Thomas Wenzler, Daniel J Mortlock, and Andrew H Jaffe. Reconstruction of total solar irradiance 1974–2009. *Astronomy & Astrophysics*, 541:A27, 2012.

[7] C Beck, R Rezaei, D Prasad Choudhary, S Gosain, A Tritschler, and RE Louis. High-resolution observations of h α spectra with a subtractive double pass. *Solar Physics*, 293(2):36, 2018.

[8] RL Blake, TA Chubb, H Friedman, and AE Unzicker. Spectral and photometric measurements of solar x-ray emission below 60 å. *Astrophysical Journal, vol. 142, p. 1*, 142:1, 1965.

[9] Thomas Robert Burnight. Soft x-radiation in the upper atmosphere. *Phys. Rev*, 76(165):19–9, 1949.

[10] Debra L. Burris, Catherine A. Pilachowski, Taft E. Armandroff, Christopher Sneden, John J. Cowan, and Henry Roe. Neutron-capture elements in the early galaxy: Insights from a large sample of metal-poor giants. *The Astrophysical Journal*, 544(1):302, nov 2000.

[11] Mats Carlsson, Bart De Pontieu, and Viggo H Hansteen. New view of the solar chromosphere. *Annual Review of Astronomy and Astrophysics*, 57(1):189–226, 2019.

[12] G Catanzaro and F Leone. Spectroscopic analysis of the sb3 system 74 aqr. *Monthly Notices of the Royal Astronomical Society*, 373(1):330–336, 2006.

[13] M Collados, R López, E Páez, E Hernández, M Reyes, A Calcines, E Ballesteros, JJ Díaz, C Denker, A Lagg, et al. Gris: the gregor infrared spectrograph. *Astronomische Nachrichten*, 333(9):872–879, 2012.

[14] Steven R Cranmer. Coronal holes. *Living reviews in solar physics*, 6(1):3, 2009.

[15] C Denker. Instrument and data analysis challenges for imaging spectropolarimetry. *Astronomische Nachrichten*, 331(6):648–651, 2010.

[16] Frank N Edmonds and Jin-Chung Hsu. A statistical analysis of nai d 1 profile fluctuations at the center of the solar disk: I. data reduction and resolvable velocities. *Solar Physics*, 83:217–232, 1983.

[17] MT Eibe, P Mein, Th Roudier, and M Faurobert. Investigation of temperature and velocity fluctuations through the solar photosphere with the na id lines. *Astronomy & Astrophysics*, 371(3):1128–1136, 2001.

[18] AH Gabriel. Measurements on the lyman alpha corona. *Solar Physics*, 21:392–400, 1971.

[19] Wei-Qun Gan, Cheng Zhu, Yuan-Yong Deng, Hui Li, Yang Su, Hai-Ying Zhang, Bo Chen, Zhe Zhang, Jian Wu, Lei Deng, et al. Advanced space-based solar observatory (aso-s): an overview. *Research in Astronomy and Astrophysics*, 19(11):156, 2019.

[20] Marina Giarrusso, Gerardo Avila, G Del Zanna, E Landi, F Leone, M Munari, G Castro, L Celona, S Gammino, D Mascali, et al. High resolution spectropolarimetry: From astrophysics to ecr plasmas. *Journal of Instrumentation*, 13(11):C11020, 2018.

[21] L Golub, M Herant, K Kalata, I Lovas, G Nystrom, F Pardo, E Spiller, and J Wilczynski. Subarcsecond observations of the solar x-ray corona. *Nature*, 344(6269):842–844, 1990.

[22] David F Gray. *The observation and analysis of stellar photospheres*. Cambridge university press, 2021.

[23] A Hofmann, K Arlt, H Balthasar, SM Bauer, W Bittner, J Paschke, E Popow, J Rendtel, D Soltau, and T Waldmann. The gregor polarimetric calibration unit. *Astronomische Nachrichten*, 333(9):854–862, 2012.

[24] Xingcheng Hu, Jinsheng Yang, Xuejun Rao, and Changhui Rao. Fabry–pérot interferometer-based tunable narrow-band imager for solar chromospheric observation: First results. *Solar Physics*, 297(6):74, 2022.

[25] Eberhart Jensen and Frank Q Orrall. Observational study of macroscopic inhomogeneities in the solar atmosphere. iv. velocity and intensity fluctuations observed in the k line. *Astrophysical Journal, vol. 138, p. 252*, 138:252, 1963.

[26] F Kneer and J Hirzberger. A fabry-perot spectrometer for high-resolution observation of the sun. *Astronomische Nachrichten: Astronomical Notes*, 322(5-6):375–378, 2001.

[27] David Kuridze, Mihalis Mathioudakis, Damian J Christian, AF Kowalski, David B Jess, Samuel DT Grant, Tomoko Kawate, PJA Simões, JC Allred, and Francis P Keenan. Observations and simulations of the na i d1 line profiles in an m-class solar flare. *The Astrophysical Journal*, 832(2):147, 2016.

[28] J Leenaarts and S Wedemeyer-Böhm. Dot tomography of the solar atmosphere-iii. observations and simulations of reversed granulation. *Astronomy & Astrophysics*, 431(2):687–692, 2005.

[29] Jorrit Leenaarts, Mats Carlsson, and L Rouppe Van Der Voort. The formation of the hα line in the solar chromosphere. *The Astrophysical Journal*, 749(2):136, 2012.

[30] James R Lemen, Alan M Title, David J Akin, Paul F Boerner, Catherine Chou, Jerry F Drake, Dexter W Duncan, Christopher G Edwards, Frank M Friedlaender, Gary F Heyman, et al. The atmospheric imaging assembly (aia) on the solar dynamics observatory (sdo). *Solar Physics*, 275:17–40, 2012.

[31] Hui Li, Bo Chen, Li Feng, Ying Li, Yu Huang, Jing-Wei Li, Lei Lu, Jian-Chao Xue, Bei-Li Ying, Jie Zhao, et al. The lyman-alpha solar telescope (lst) for the aso-s mission—i. scientific objectives and overview. *Research in Astronomy and Astrophysics*, 19(11):158, 2019.

[32] Tine Libbrecht. *The diagnostic potential of the He I D3 spectral line in the solar atmosphere*. PhD thesis, Department of Astronomy, Stockholm University, 2019.

[33] Tine Libbrecht, Jayant Joshi, Jaime de la Cruz Rodríguez, Jorrit Leenaarts, and Andrés Asensio Ramos. Observations of ellerman bomb emission features in he i d3 and he i 10 830 å. *Astronomy & Astrophysics*, 598:A33, 2017.

[34] Zhong Liu, Jun Xu, Bo-Zhong Gu, Sen Wang, Jian-Qi You, Long-Xiang Shen, Ru-Wei Lu, Zhen-Yu Jin, Lin-Fei Chen, Ke Lou, et al. New vacuum solar telescope and observations with high resolution. *Research in Astronomy and Astrophysics*, 14(6):705, 2014.

[35] J Löhner-Böttcher, W Schmidt, R Schlichenmaier, H-P Doerr, Tilo Steinmetz, and Ronald Holzwarth. Absolute velocity measurements in sunspot umbrae. *Astronomy & Astrophysics*, 617:A19, 2018.

[36] DJ McComas, HA Elliott, NA Schwadron, JT Gosling, Ruth M Skoug, and BE Goldstein. The three-dimensional solar wind around solar maximum. *Geophysical research letters*, 30(10), 2003.

[37] Taro Morimoto and Hiroki Kurokawa. A Method for the Determination of 3-D Velocity Fields of Disappearing Solar Filaments. *Publications of the Astronomical Society of Japan*, 55(2):503–518, 04 2003.

[38] Daniel Müller, OC St Cyr, Ioannis Zouganelis, Holly R Gilbert, R Marsden, T Nieves-Chinchilla, E Antonucci, Frédéric Auchere, D Berghmans, TS Horbury, et al. The solar orbiter mission-science overview. *Astronomy & Astrophysics*, 642:A1, 2020.

[39] Aimee A Norton, J Pietarila Graham, RK Ulrich, J Schou, S Tomczyk, Y Liu, Bruce W Lites, A López Ariste, RI Bush, H Socas-Navarro, et al. Spectral line selection for hmi: A comparison of fe i 6173 å and ni i 6768 å. *Solar Physics*, 239:69–91, 2006.

[40] CFR OHLICH. Solar irradiance variability since 1978. *Space Science Reviews*, 125:53–65, 2006.

[41] W Dean Pesnell, B J Thompson, and PC Chamberlin. *The solar dynamics observatory (SDO)*. Springer, 2012.

[42] KG Puschmann. Modern solar facilities–advanced solar science, 45-50 f. kneer, kg puschmann, ad wittmann (eds.) universitätsverlag göttingen 2007. In *Modern Solar Facilities-Advanced Solar Science: Proceedings of a Workshop Held at Göttingen, September 27-29, 2006*, page 45. Universitätsverlag Göttingen, 2007.

[43] Brian D Ramsey, Robert A Austin, and Rudolf Decher. Instrumentation for x-ray astronomy. *Space science reviews*, 69:139–204, 1994.

[44] Pierre Rochus, Frederic Auchere, David Berghmans, Louise Harra, W Schmutz, Udo Schühle, P Addison, T Appourchaux, R Aznar Cuadrado, D Baker, et al. The solar orbiter eui instrument: the extreme ultraviolet imager. *Astronomy & Astrophysics*, 642:A8, 2020.

[45] R Rosner, L Golub, B Coppi, and GSz Vaiana. Heating of coronal plasma by anomalous current dissipation. *Astrophysical Journal, Part 1, vol. 222, May 15, 1978, p. 317-332. Research supported by the Smithsonian Institution;*, 222:317–332, 1978.

[46] RJ Rutten, RH Hammerschlag, FCM Bettonvil, P Sütterlin, and AG De Wijn. Dot tomography of the solar atmosphere-i. telescope summary and program definition. *Astronomy & Astrophysics*, 413(3):1183–1189, 2004.

[47] RJ Rutten and RIr Kostik. Empirical nlte analyses of solar spectral lines. iii-iron lines versus lte models of the photosphere. *Astronomy and Astrophysics, vol. 115, no. 1, Nov. 1982, p. 104-114.*, 115:104–114, 1982.

[48] RJ Rutten, Jorrit Leenaarts, LHM Rouppe van der Voort, AG De Wijn, M Carlsson, and Viggio Hansteen. Quiet-sun imaging asymmetries in na i d1 compared with other strong fraunhofer lines. *Astronomy & Astrophysics*, 531:A17, 2011.

[49] Goran B Scharmer, Klas Bjelksjo, Tapio K Korhonen, Bo Lindberg, and Bertil Petterson. The 1-m swedish solar telescope. In *Innovative telescopes and instrumentation for solar astrophysics*, volume 4853, pages 341–350. SPIE, 2003.

[50] Philip Hanby Scherrer, Jesper Schou, RI Bush, AG Kosovichev, RS Bogart, JT Hoeksema, Y Liu, TL Duvall, J Zhao, AM Title, et al. The helioseismic and magnetic imager (hmi) investigation for the solar dynamics observatory (sdo). *Solar Physics*, 275:207–227, 2012.

[51] W Schmidt, O Von der Lühe, R Volkmer, C Denker, SK Solanki, H Balthasar, N Bello Gonzalez, Th Berkefeld, M Collados, A Fischer, et al. The 1.5 meter solar telescope gregor. *Astronomische Nachrichten*, 333(9):796–809, 2012.

[52] Sami K Solanki, JC del Toro Iniesta, Joachim Woch, A Gandorfer, Johann Hirzberger, A Alvarez-Herrero, T Appourchaux, V Martínez Pillet, I Pérez-Grande, E Sanchis Kilders, et al. The polarimetric and helioseismic imager on solar orbiter. *Astronomy & Astrophysics*, 642:A11, 2020.

[53] O Steiner, M Franz, N Bello González, Ch Nutto, R Rezaei, V Martínez Pillet, JA Bonet Navarro, JC del Toro Iniesta, V Domingo, SK Solanki, et al. Detection of vortex tubes in solar granulation from observations with sunrise. *The Astrophysical Journal Letters*, 723(2):L180, 2010.

[54] Lucas A Tarr, Adam R Kobelski, Sarah A Jaeggli, Momchil Molnar, Gianna Cauzzi, and Kevin P Reardon. Spatio-temporal comparisons of the hydrogen-alpha line width and alma 3 mm brightness temperature in the weak solar network. *Frontiers in Astronomy and Space Sciences*, 9:978405, 2023.

[55] LHM Rouppe van der Voort. Penumbral structure and kinematics from high-spatial-resolution observations of k. *Astronomy & Astrophysics*, 389(3):1020–1038, 2002.

[56] Jorge E Vernazza, Eugene H Avrett, and Rudolf Loeser. Structure of the solar chromosphere. iii-models of the euv brightness components of the quiet-sun. *Astrophysical Journal Supplement Series, vol. 45, Apr. 1981, p. 635-725.*, 45:635–725, 1981.

[57] Gregal JM Vissers, Luc HM Rouppe van der Voort, and Robert J Rutten. Automating ellerman bomb detection in ultraviolet continua. *Astronomy & Astrophysics*, 626:A4, 2019.

[58] O Von Der Lühe, R Volkmer, TJ Kentischer, and R Geißler. The gregor broad-band imager. *Astronomische Nachrichten*, 333(9):894–900, 2012.

[59] A Vourlidas, B Sanchez Andrade-Nuño, E Landi, S Patsourakos, L Teriaca, U Schühle, CM Korendyke, and I Nestoras. The structure and dynamics of the upper chromosphere and lower transition region as revealed by the subarcsecond vault observations. *Solar Physics*, 261:53–75, 2010.

[60] Thomas N Woods, FG Eparvier, R Hock, AR Jones, D Woodraska, D Judge, L Didkovsky, J Lean, J Mariska, H Warren, et al. Extreme ultraviolet variability experiment (eve) on the solar dynamics observatory (sdo): Overview of science objectives, instrument design, data products, and model developments. *The solar dynamics observatory*, pages 115–143, 2012.

[61] Chenglin Xu, Zhongquan Qu, Xiaoyu Zhang, Chunlan Jin, and Xiaoli Yan. Polarimeter with two ferroelectric liquid-crystal modulators attached to the yunnan solar tower. *Applied optics*, 45(33):8428–8433, 2006.

[62] Harold Zirin. Astrophysics of the sun. *Cambridge: University Press*, 1988.